

# Automated Detection of Double Nuclei Galaxies using *GOTHIC* and the Discovery of a Large Sample of Dual AGN

Anwesh Bhattacharya<sup>1</sup>, Nehal C. P.<sup>2</sup>, Mousumi Das<sup>3</sup>, Abhishek Paswan<sup>3,4</sup>, Snehanshu Saha<sup>5</sup>\*, Fran<sup>coise Combes<sup>6</sup></sup>

<sup>1</sup>Dept. of Physics and CSIS, Birla Institute of Technology & Science, Pilani, India

<sup>2</sup>Dept. of Physics, Indian Institute of Science Education and Research, Bhopal

<sup>3</sup>Indian Institute of Astrophysics, Bangalore

<sup>4</sup>Department of Physics, University of Allahabad, India

<sup>5</sup>CSIS and APPCAIR, Birla Institute of Technology & Science, Goa, India

<sup>6</sup>Observatoire de Paris, LERMA, Coll $ège de France, PSL University, Sorbonne University, CNRS, Paris, France$

Accepted XXX. Received YYY; in original form ZZZ

## ABSTRACT

We present a novel algorithm to detect double nuclei galaxies (DNG) called **GOTHIC** (Graph-Boosted iterated Hill Climbing) — that detects whether a given image of a galaxy has two or more closely separated nuclei. Our aim is to detect samples of dual or multiple active galactic nuclei (AGN) in galaxies. Although galaxy mergers are common, the detection of dual AGN is rare. Their detection is very important as they help us understand the formation of supermassive black hole (SMBH) binaries, SMBH growth and AGN feedback effects in multiple nuclei systems. There is thus a need for an algorithm to do a systematic survey of existing imaging data for the discovery of DNGs and dual AGN. We have tested GOTHIC on a known sample of DNGs and subsequently applied it to a sample of a million SDSS DR16 galaxies lying in the redshift range of  $z=0$  to 0.75 approximately, and have available spectroscopic data. We have detected 159 dual AGN in this sample, of which 2 are triple AGN systems. Our results show that dual AGN are not common, and triple AGN even rarer. The color (u-r) magnitude plots of the DNGs indicate that star formation is quenched as the nuclei come closer and as the AGN fraction increases. The quenching is especially prominent for dual/triple AGN galaxies that lie in the extreme end of the red sequence.

**Key words:** galaxies : interactions – galaxies : active – galaxies : nuclei – galaxies : evolution – techniques: image processing – methods: numerical

## 1 INTRODUCTION

Galaxy mergers are the main mechanism for the hierarchical growth of galaxies in our low redshift universe (White & Rees 1978; Patton et al. 2020). Depending upon the gas content of galaxies, gas rich mergers can lead to substantial amounts of star formation, resulting in starbursts and ultraluminous infrared galaxies (ULIRGs) (Sanders & Mirabel 1996). Dry or gas free mergers of elliptical and S0 galaxies do not result in star formation but lead to the growth of more massive early type galaxies (Thomas et al. 2005). As galaxies merge, the bulges and nuclei of the individual galaxies come closer leading to the formation of dual or even multiple nuclei systems that are often enclosed within a single galaxy envelope (Capelo et al. 2017). In the process, one or more of the supermassive black holes (SMBHs) in the galaxy nuclei may start accreting mass leading to the formation of active galactic nuclei (AGN) (Shlosman et al. 1990; Peterson 1997). Alternatively, large amounts of gas may fall into the nuclear regions of the merging galaxies triggering nuclear starburst activity (Kim et al. 2021).

Thus, double nuclei galaxies can host AGN pairs, AGN-starburst

pairs or individual star forming nuclei in their centers (Rubinur et al. 2019). When two or more AGN are found in a merger remnant and are separated by  $<10$  kpc, it is often termed as a dual AGN (DAGN) system, although the definition varies in the literature and can include AGN at separations of upto  $\sim 50$  kpc (Koss et al. 2012). Triple AGN systems have also been detected in small groups of merging galaxies (Yadav et al. 2021) which suggests that multiple AGN systems maybe more common than we think. In fact simulations have shown that minor mergers can lead to many massive black holes (MBHs) that are spatially offset from the central galaxy nucleus; such MBHs are called "wandering black holes", since they do not appear to be in the process of merging with the nuclear SMBH (Bellovary et al. 2010; Ricarte et al. 2021). A few wandering MBHs have been detected (Greene et al. 2021; Reines et al. 2020). If an AGN pair is separated by only a few parsecs or  $<1$  kpc, it is termed as a binary AGN (BAGN). The number of DAGN identified till now is  $<100$  (Rubinur et al. 2018; Stemo et al. 2021) and the number of detected binary AGN is  $<5$  (Kharb et al. 2017a). These numbers are small compared to the total fraction of AGN detected in galaxies at low redshifts. Since galaxy mergers are common, this suggests that there is a large population of dual/multiple AGN systems that have not yet been detected.

\* Corresponding author - snehanshu.saha@ieee.org

Most of the early detections of DAGN in the literature were serendipitous, and were discovered during galaxy surveys of emission line galaxies and merger remnants (Komossa et al. 2003) or radio observations of compact sources (Rodriguez et al. 2006). Later studies used samples of double peaked AGN emission line galaxies (DPAGN) to search for DAGN (Zhou et al. 2004; Rubinur et al. 2019; Maschmann et al. 2020). However, DPAGN can also be due to AGN outflows or rotating disks (Kharb et al. 2017b). Recent studies have shown that one of the best ways to detect DAGN is by using a parent sample of dual nuclei galaxies and then identifying the nature of their nuclei using multi-wavelength observations (De Rosa et al. 2019). However, the latest surveys of galaxy pairs are either too small or the nuclei separations are too large to be defined as dual nuclei systems (Patton et al. 2016).

There are several reasons why we need to find more dual or multiple AGN systems. One of the most important reasons is that they represent the first stage in the formation of SMBHs pairs. At distances of several Mpc beyond the local universe, the only way to detect SMBHs is via the radiation emitted from AGN activity. Although the gravitational radiation from SMBH pairs is emitted only when they are separated by less than a parsec, a large sample of DAGN will help us understand how they form and evolve. So revealing the frequency and nature of SMBH pairs is the first step in understanding the low frequency (nanohertz) gravitational waves radiated by inspiralling SMBHs (Aggarwal et al. 2019; Goulding et al. 2019; Shannon et al. 2015). Secondly, although multiple/dual AGN are rare, it has been shown that galaxy mergers are important triggers of AGN activity and the formation of DAGN, both of which can lead to nuclear star formation and SMBH growth. Simulations have suggested that merger-triggered AGN may dominate SMBH growth (Hopkins et al. 2014). Finally, SMBH pairs or clusters will affect the AGN feedback and stellar winds/outflows associated with galaxy mergers, which can result in the growth of the circumgalactic medium (CGM) around galaxies (Fielding et al. 2020; Davies et al. 2020). Multiple AGN can give rise to stronger winds and outflows, producing additional feedback effects as observed in nearby DAGN (Mazzarella et al. 2012; Rubinur et al. 2020). Hence, large samples of DAGN are essential for fully understanding the role of mergers in SMBH growth and galaxy evolution.

In this paper we present an automated search for dual/multiple nuclei in merging and interacting galaxies, using an algorithm called *GOTHIC* that detects such systems using optical images (Bhattacharya et al. 2020). We applied *GOTHIC* to SDSS images and derived a large sample of double and multiple nuclei in closely interacting galaxies and merger remnants. Our broad goal is to detect a large sample of dual or multiple nuclei that can be used to detect DAGN (or even multiple AGN systems). In the following section we first review previous studies that search for galaxy pairs and then build the case for the need of a large catalog of dual nuclei galaxies (DNGs). We also discuss the initial testing sample that was used for evaluating the detection rate of the algorithm. In Section 3, we describe the algorithm, which is heuristic in nature, and we provide justifications for its design and the decisions adopted in the procedure. In order to establish whether the algorithm performs well, we tested it against a known sample of DNGs and found that its detection accuracy is  $> 95\%$ . The details of the verification can be found in Section 4. We subsequently performed a blind search by applying the algorithm on a large sample of 1 million galaxies and detected 100,000 candidate DNGs. We filtered this sample and manually analyzed the final, smaller DNG candidate sample in Section 5 and Section 6. We then present the DNGs in a catalogue and discuss their properties. We have separated out the dual and multiple AGN in the sample and

discussed the nature of the host galaxies. Finally, we conclude with a discussion of the impact of our study on understanding DAGN and galaxy mergers in Section 7 and Section 8.

## 2 WHY AUTOMATE THE SEARCH OF DOUBLE NUCLEI GALAXIES?

### 2.1 Previous Studies and our Motivation

Large samples of galaxy pairs have been previously derived in the literature from imaging or spectroscopic surveys, by selecting the nearest neighbor galaxies. This was usually done by constructing radial bins around galaxies and selecting neighboring galaxies that lie within specific radii from the target galaxy (e.g.  $R < 2$  Mpc) (Bustamante et al. 2020). Alternatively, differences in systemic velocities between a target galaxy and its neighbors were used to derive the closest neighbor (Maschmann et al. 2020). Although this method did select galaxy pairs, it was mainly aimed at detecting the tidal features in interacting galaxies (Ellison et al. 2010) and the effect of galaxy interactions on star formation (Barton et al. 2000; Patton & Atfield 2008). Most of the galaxy pairs that were detected in these surveys were separated by several megaparsec (Mpc) distances, and hence these samples basically represent galaxies interacting at a distance but not actually merging. Many of these surveys also have constraints on the mass ratios of the two galaxies and contain distant pairs and not close galaxy pairs (Bustamante et al. 2020). These methods are thus biased towards detecting galaxies interacting at a distance rather than merger remnants that contain two or more nuclei encased in a single envelope or closely interacting galaxies.

There have recently been several studies of galaxy pairs in cosmological simulations. These studies use hydrodynamical simulations to build samples of mergers which are then used to build mock samples upon which an image-classification scheme is developed. However, some studies suggest that mock images may result in poor performance in merger classifications (Bottrell et al. 2019). Others have performed convolutional neural network (CNN) training on processed isolated galaxy images (e.g. IllustrisTNG) for the task of automated merger classification (Bickley et al. 2021; Nelson et al. 2021). They obtain a sample with a purity of only 6% due to the intrinsic rarity of galaxy mergers. Thus, there is clearly some difficulty in building a clean observational sample of galaxy mergers using simulations (Nevin et al. 2019). Studies have also compared the efficiency of using stellar kinematics versus visual images and found that visual identification is better (Bottrell et al. 2021). This is clearly demonstrated in (Blumenthal et al. 2019) where samples of *Visually Identified Pairs* (VIP) are presented using simulated images from IllustrisTNG.

Thus there is a need for an algorithm and pipeline that can sift through large optical or near-infrared (NIR) imaging surveys of real galaxies and extract double/multiple galaxy nuclei efficiently with no bias with respect to spatial separations, galaxy mass ratios or redshift ranges of the galaxies. Such a method will be computationally more efficient compared to counting nearest neighbors in radial bins. It is with this aim in mind that we have developed an algorithm that can detect dual nuclei systems at kiloparsec (kpc) scale separations from an optical survey and identify a pool of dual nuclei systems that can be used to study galaxy mergers and detect candidate dual/multiple AGN systems. In the following section we discuss the training sample of dual nuclei that we have used in our study.

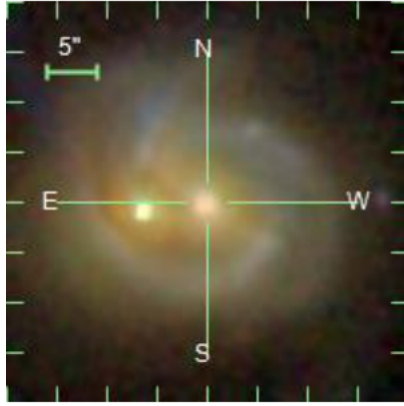


**Figure 1.** Color composite SDSS image of MRK 739 showing clearly the two nuclei.

## 2.2 The Trial Sample

To estimate the efficiency of any code that is aimed at identifying certain types of sources, it is essential to have a sample that the code can be tested on. A large catalog is also necessary to do statistical studies of dual nuclei galaxies, compare with galaxy merger models and detect DAGN. The Gimeno Catalog (GC hereafter) (Gimeno et al. 2004) presents a compiled sample of 107 DNGs from previously existing catalogs. They have also used ESO plates to catalogue the sources. Further studies by Mezcua et al. (2014) used GC but selected those with entries present in SDSS DR8 and finalized on a sample of 60 dual nuclei systems. After rejecting galaxies that are difficult to study due to noisy images, they performed the PSF fitting of 52 galaxies.

A good example of the type of sources that we are interested in detecting is MRK 739 (Figure 1). It was first studied in detail by Koss et al. (2011) where it was confirmed to host a dual AGN. It was more recently studied by Tubín et al. (2021) who identified the western and eastern nuclei to be on their ongoing first passage. The construction of our algorithm is targeted towards finding galaxies that resemble the visual features of MRK 739 i.e. there should basically be at least two distinct bulges.

## 3 DESCRIPTION OF THE PROCEDURE

To determine whether a galaxy is closely interacting or merging with another galaxy or is a dual nuclei galaxy (DNG) we need to first have image cutouts of galaxies from SDSS. Figure 1 is an example of a color composite image of a DNG in the SDSS display in [object explorer](#). It is a  $40'' \times 40''$  square-cutout centred on the coordinates with which the `objID` of the object is associated. A successful algorithm for DNG detection must be able to identify the light envelope of one galaxy or two close galaxies, and detect the presence of two distinct bulges if any. In practice, however, not every `objID` of a galaxy in the SDSS database faithfully corresponds to a galaxy *i.e.*, some IDs correspond to stars, QSOs, or blank patches of sky with no visible object in its vicinity. So the detection procedure must carefully handle mislabelled galaxies. The incorrectness in the *ground truth* of SDSS labels has been documented in the study by Makhija et al. (2019).

Another constraint is the superposition of background images with foreground galaxies. It is possible to conceive a scenario where a foreground star is aligned with an otherwise single-nucleus galaxy. Such galaxies must not be categorized as DNGs, else it would

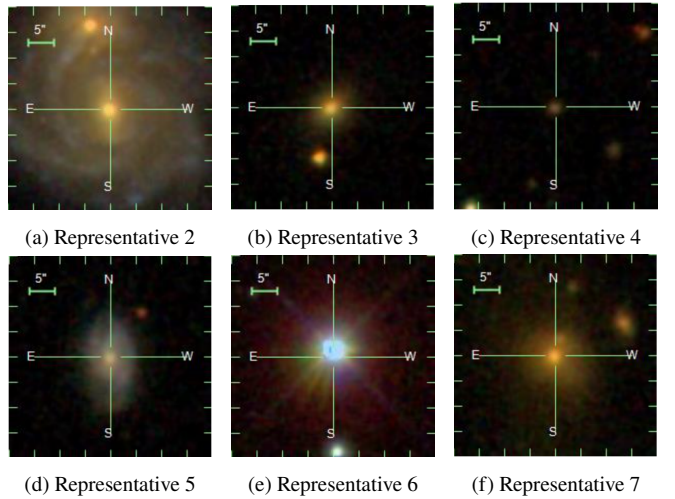


**Figure 2.** Representative samples of the SDSS images of the different types of potential DNG.

increase the number of false detections. One of the ways to prevent these is to use only a spectroscopic sample, so that the redshift ( $z$ ) information for each nucleus can be included. If the sources are widely separated in redshift space (e.g.  $z=0.1$  and  $0.001$ ), then the sources cannot be a DNG. In Table 1, we present a list of `objID`s from SDSS that are representative of the images of galaxies seen in practice. In the remainder of this paper, we refer to the  $n^{\text{th}}$  representative galaxy as "Rep  $n$ ".

We describe our detection procedure by demonstrating how it processes these examples. The pseudocode for each of the necessary sub-procedures has been included in the Appendix. For each sub-procedure below, we categorically state the representatives chosen for its demonstration.

### 3.1 Image Normalization and Smoothing

#### Representative Chosen - 1

Every object must be appropriately treated so that it is amenable for classification. Using `astropy` (Price-Whelan et al. 2018), a  $40''$  cutout centred on an object coordinates was performed. The raw cutout of rep 1 is shown in Figure 3a. However, the light envelope of the galaxy and the dark background are not amenable contrasted for further analysis. The nuclei at the centre of the galaxy is faint and the body of the galaxy is not visible.

To solve this issue, we performed a log normalization of all pixel values in the cutout followed by appropriate scaling of the image within the range of  $[0, 255]$ . Subsequently, we performed a gaussian smoothing using kernels with standard deviations of  $(\sigma_x, \sigma_y) = (5, 5)$ . The resulting image is shown in figure Figure 3b.

### 3.2 Bounding the Galaxy via Edge Detection and Convex Hull

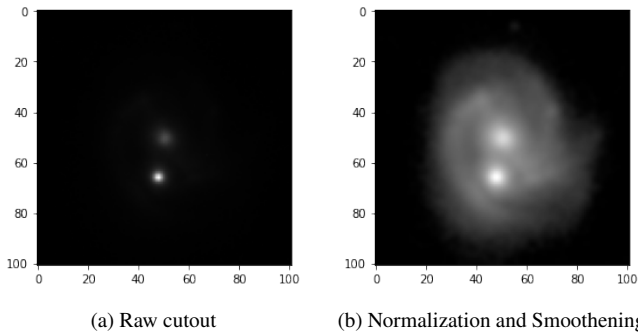
#### Representatives chosen - 1, 5, 7

Determining whether a galaxy is a DNG requires a reliable detection of two individual bright bulges within a galaxy envelope. Hence, it is important to determine the light envelope of the galaxy within which the search for dual peaks will take place. We used the Canny (Canny 1986) edge detection technique, which utilizes

[b]

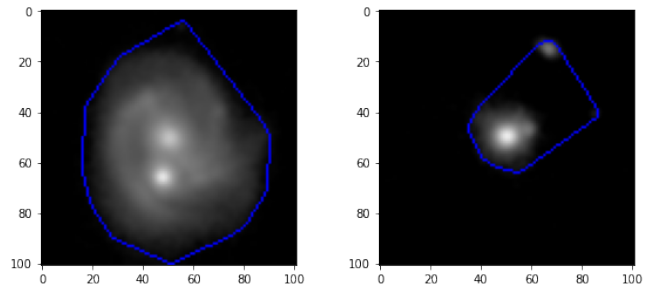
**Table 1.** List of representative objIDs

No.	objID	Common Name	Description	Figure
1	1237667734504407133	MRK 739	Standard example of DNG	1
2	1237666301638279613	UGC 3141	DNG with nuclei far apart. This example has been chosen to demonstrate the limits of <i>GOTHIC</i> .	2a
3	1237651752385708153	2MASX J09520344+0052159	Single nucleus galaxy with a star in the foreground. Such samples are potential false positives.	2b
4	1237648720143647179	SDSS J095203.44+005216.3	The frame does not contain sufficiently bright objects which can be detected by <i>GOTHIC</i> . Many objIDs in the blind search corresponding to such frames.	2c
5	1237650794609246465	SDSS J094333.74-010551.3	Single nucleus galaxy. These are the most commonly encountered objects in a blind search. Hence it's important to verify that they are reliably identified.	2d
6	1237648720688971816	SDSS J111508.35-003125.0	Star mislabelled as a galaxy in SDSS which we frequently encountered in the blind search. Hence it is a clear representative.	2e
7	1237650796756926591	2MASS J09450600+0034516	Two galaxies in the same line of sight. Similar to representative 3, this is a potential source of false-positives.	2f



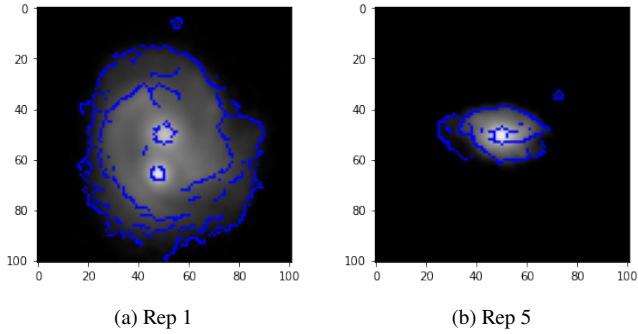
(a) Raw cutout

(b) Normalization and Smoothening

**Figure 3.** The raw and normalized SDSS cutouts for rep 1

(a) Rep 1

(b) Rep 7

**Figure 5.** Convex Hull of the Edges**Figure 4.** Edges detected by Canny

the Sobel (Vincent & Folorunso 2009) operator to approximate the values of  $\frac{\partial}{\partial x}$  and  $\frac{\partial}{\partial y}$  of each pixel in the image. Subsequently, the magnitude  $\sqrt{\left(\frac{\partial}{\partial x}\right)^2 + \left(\frac{\partial}{\partial y}\right)^2}$  is computed which represents how strongly a particular pixel is an edge.

For example, Figure 4a and Figure 4b show the edges detected by Canny (in blue) for reps 1, 5 respectively. It is to be noted that Canny detects edges within the light envelope of the galaxy. This is expected since the Sobel operator measures the difference between neighboring pixel values at a given pixel coordinate. Generally, light profiles of galaxies in SDSS are not smooth and this causes sizeable differences between pixel values within the light envelope which are mistakenly detected as edges.

We reiterate that the Gaussian Smoothing step in Section 3.1 is

necessary as it reduces the detection of false edges within the light envelope. If the smoothing step were skipped, the Canny algorithm would detect far more edges than necessary. On the other hand, excessive smoothing using higher values of  $(\sigma_x, \sigma_y)$  would lead to no edges being detected. To resolve this issue, we find the convex hull of the pixel coordinates that have been detected as edges. The hulls for reps 1 and 7 are shown in Figure 5a and Figure 5b respectively. Formally, the convex hull of a set of points  $\mathcal{S} = \{(x, y)\}$  in 2-D is the smallest convex polygon that contains in its interior all points in  $\mathcal{S}$ . Sklansky (1982) and Cormen et al. (2009) present an overview of the Convex Hull problem and efficient algorithms for computing it.

Note that the hull in Figure 5b encloses a neighboring object. However, it is clear that this object is not of interest to us. In other words, we assume that the enclosed hull contains more objects that are of interest to us merely due to them being on the same line of sight. Since our cutout size is  $40''$ , it is reasonable to expect that any arbitrary object would have many other objects in their line of sight and they need to be handled carefully. Otherwise it will lead to unnecessarily high false-positive detections. The sub-procedures in Section 3.3, Section 3.4 and part of Section 3.6 are dedicated to deal with such "line of sight" scenarios.

### 3.3 Numerical Fitting of the Galaxy Light Profile

#### Representatives Chosen - 1

Since the convex hull might enclose a larger area than the object of interest, it needs to be ascertained what portion of the image within the hull resembles a galaxy envelope. In Figure 5b, approximately

one half of the hull (at the centre of the square image) contains the galaxy. This patch of light needs to be identified from the remainder of the hull. Selecting the object of interest from the hull is manually easy for humans to perform, however, a formal procedure for doing so becomes necessary as we aim to automatically search for DNGs.

We make the assumption that the enclosed hull would always contain our galaxy of interest as well as other objects within the line of sight. The light profile of galaxies typically follow a distribution given by Sérsic (1963). This fact can be exploited to develop a procedure that separates a galaxy from the rest of the hull. Hence, we hypothesize that the pixel values in the hull will follow the Sérsic distribution. The expression for the Sérsic profile is as follows

$$\log I(R) = \log I_0 - k R^{\frac{1}{n}} \quad (1)$$

where  $I(R)$  is the light intensity of a galaxy as a function of the radial distance  $R$  from the galactic centre. The parameter  $n$  is known as the Sérsic index and it characterizes the overall shape of the light distribution. Caon et al. (1993) states that  $1 \leq n \leq 15$  fits the light profile of most galaxies. However, we have found that setting  $0.25 \leq n \leq 15$  works better in practice.

Although the Sérsic profile is expressed as a function of galactic radius, we do not have any radial information from the smoothed image or the convex hull. In fact, one would first need to identify a galactic centre from which the radius would be measured. We can use the center (0,0) of the cutout as the galactic centre since SDSS cutouts are centred on the object of interest. Subsequently, the radius  $R$  of a point  $(x, y)$  is measured as the Manhattan distance from the centre *i.e.*,  $R = |x| + |y|$ . It is possible to compute the histogram (*i.e.*, frequency) of pixel values  $|x| + |y|$  within the hull. This allows us to posit the light profile as a function of the frequency  $f$ , instead of  $R$ , and we compute the frequency profile  $I(f)$ . The relation used to transform from  $R$  to  $f$  is  $f = 4R$ . The derivation and justification of this relation can be found in (Appendix Section A1).

We denote the histogram function of the smoothed image as  $F \equiv F(p)$  which translates pixel values to their corresponding frequency values. Let the inverse histogram be  $P \equiv P(f)$  that translates frequency numbers to pixel values of the smoothed image. The FITS files in SDSS report pixel values in a unit of flux called nanomaggies. It is these raw pixel values that are log-normalized and hence  $P(f)$  would be in the form of (Equation 1) apart from a constant additive factor. Hence, the  $P(f)$  would have the form

$$P(f; k, n) = P_{max} - k \left( \frac{f}{4} \right)^{\frac{1}{n}} \quad (2)$$

The term  $P_{max}$  is the largest pixel value within the hull. The form of (Equation 2) implicitly assumes that the pixel with the maximum value belongs to our object of interest and not a neighboring object. However, in practice, this assumption being false does not affect significantly our pipeline because (Equation 2) is numerically fit to the histogram data from the hull. Naturally, the process of numerical fitting averages over all possible errors in the data, and such errors would be present even if our assumption on the maximum pixel value were true.

$P(f)$  is numerically fitted to the observed histogram to obtain the best-fit values for its parameters  $k, n$ . We use the `optimize.curve_fit` function from `scipy` (Virtanen et al. 2020) to perform the numerical fitting. We show the fitted curve to the observed histogram of rep 1 in Figure 6. The blue dots are the observed pixel values from the smoothed image and the teal line is the numerically fitted curve  $P(f)$ .

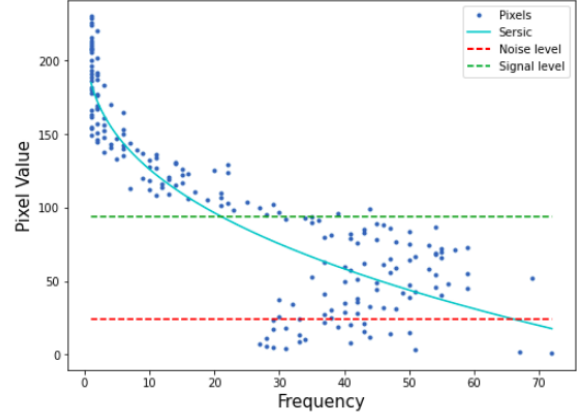


Figure 6. Rep 1 Sérsic Fit

### 3.4 Determination of the Search Region

Representatives Chosen - 1, 5, 7

After the curve  $P(f)$  has been fitted to the histogram, it remains to be determined what pixel value separates the galaxy envelope from the background. With respect to the function  $P(f)$ , pixels at that frequency value are taken as the cutoff which captures 95% of the total integrated light. In formal terms, a typical  $P(f)$  curve is a function of  $f$  from 0 to some maximum frequency value  $f_{max}$ . We define the following function

$$I_{int}(f) = \int_0^f P(f') df' \quad (3)$$

The total integrated light would be

$$I_{total} = I_{int}(f_{max}) \quad (4)$$

As per our definition, The cutoff level would then be  $P(f_{95})$  where  $f_{95}$  satisfies

$$I_{int}(f_{95}) = 0.95 \times I_{total} \quad (5)$$

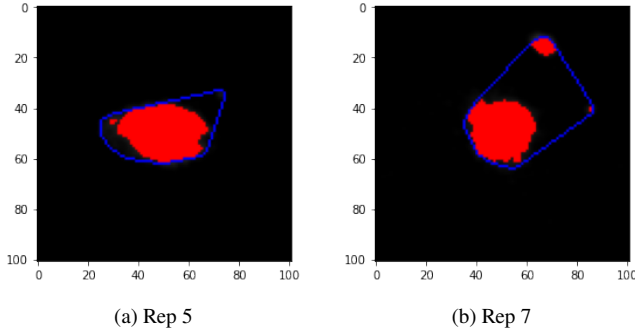
Analogously, we also define a *signal level* as the corresponding pixel value to the frequency up to which 50% of the total integrated is captured. With reference to Figure 6, the red line corresponds to the cutoff level and the green line is the signal level. The latter, although not used in determining the search region, is used in the final classification phase (Section 3.6). To perform the numerical integration, we used the composite trapezoidal rule (Talvila & Wiersma 2012) whilst dividing the range of  $[0, f_{max}]$  into 10,000 steps.

Figure 7a and Figure 7b show the pixel values above the determined cutoff level in red. This is the search region where we test for the presence of dual peaks of light. Note that the region in red is a subset of the region enclosed by the hull, and hence, our numerical fitting technique is successfully able to determine the galaxy envelope. However, neighboring objects are mistakenly included at times within the envelope since their pixel values are above the cutoff (Figure 7b). The techniques in the subsequent sections handle such scenarios.

### 3.5 Iterated Hill Climbing

Representatives chosen - 1, 2, 3

Having identified the galaxy envelope, we need to test for the

**Figure 7.** Search Region

presence of dual peaks of light which is characteristic of a DNG. However, a robust peak finding algorithm is first essential. We used a variant of the traditional hill-climbing algorithm to find the peaks. The idea is to start at a random pixel in the search region and then find the neighboring pixel which has the greatest pixel value. This process is repeated until no neighbor with a higher pixel value can be found. The final pixel at the end of this iterative process is reported to be the peak, provided the pixel value of the peak is greater than the *signal* level (Section 3.4) and the SNR ratio at the peak is  $> 3$ . To determine the noise level in the SNR calculation, we averaged over a  $3 \times 3$  grid of pixel values outside the convex hull. The region outside the hull has been considered for the noise calculation as it represents the ambient background.

Although we have performed gaussian smoothing prior to the hill climbing, no image is ideal and there are residual non-uniformities and noise. As a result, the peak found by hill climbing is sensitive to the randomly initialized starting point *i.e.*, different starting points may lead to different peaks. To eliminate such uncertainties, we repeat 1,000 instances of the hill-climbing subroutine initialized at random starting points and enlist all peaks thus found.

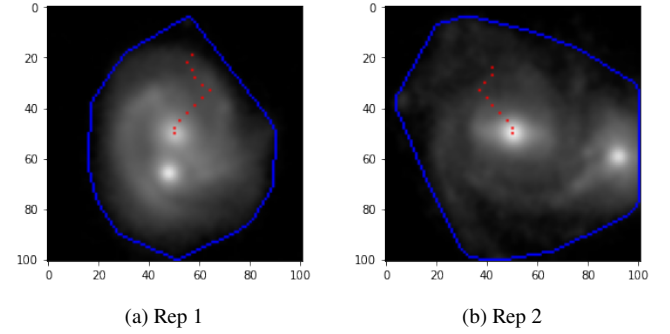
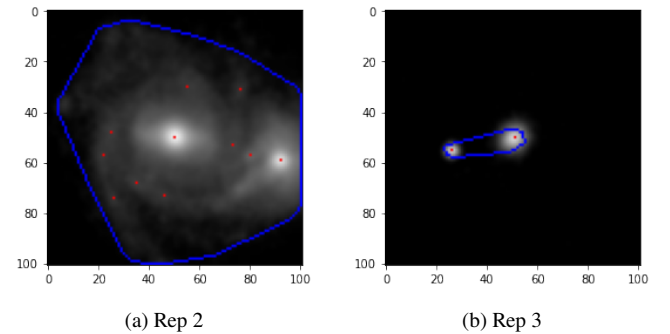
**Figure 8a** and **Figure 8b** show how one random point ascends up to the peak via hill climbing. In both cases, the initialized point is near the edge of the galaxy envelope and takes small steps until it reaches the peak at one of the nuclei. There were 10 steps taken to reach a peak in the former, and 9 steps in the latter; each step has been marked by a red pixel. **Figure 9a** and **Figure 9b** show the peaks (marked in red) obtained by repeating hill climbing process for reps 2, 3 respectively. Rep 2 (**Figure 9a**) has peaks scattered across the envelope due to residual non-uniformities in the smoothed image. Although we perform 1,000 hill climbs, only the unique peaks are reported. There are other conditions used to safely eliminate some peaks and this simplifies the classification process in the later subroutines. These criteria have been mentioned in the Appendix, along with pseudocode for the hill climbing algorithm (Appendix Section A2).

As mentioned previously, **Figure 9a** has multiple reported peaks within the galaxy envelope due to non-uniformity. Moreover, **Figure 9b** has two peaks which clearly belong to two distinct objects and such cases are a potential source of false positives. The techniques presented in Appendix Section A3 are dedicated to such cases.

### 3.6 Final Classification

**Representatives Chosen - 2, 3**

To provide the final verdict for whether a galaxy is single or double-nuclei, we use a simple criteria as follows

**Figure 8.** Trace of Hill Climb**Figure 9.** Peaks for 1000 instances of Hill Climb

**Case 1** - If no peak is found by iterated hill climbing, the source is discarded.

**Case 2** - If one peak is found, then the galaxy is a single nucleus galaxy.

**Case 3** - If the number of peaks found is  $\geq 2$ , then we have two sub-cases based on how the peaks are distributed in the various *connected-components* of the search region

- *Subcase 3.1* - If the two brightest peaks are in the same component, then the galaxy is double nuclei. Otherwise it is judged as a single nucleus.

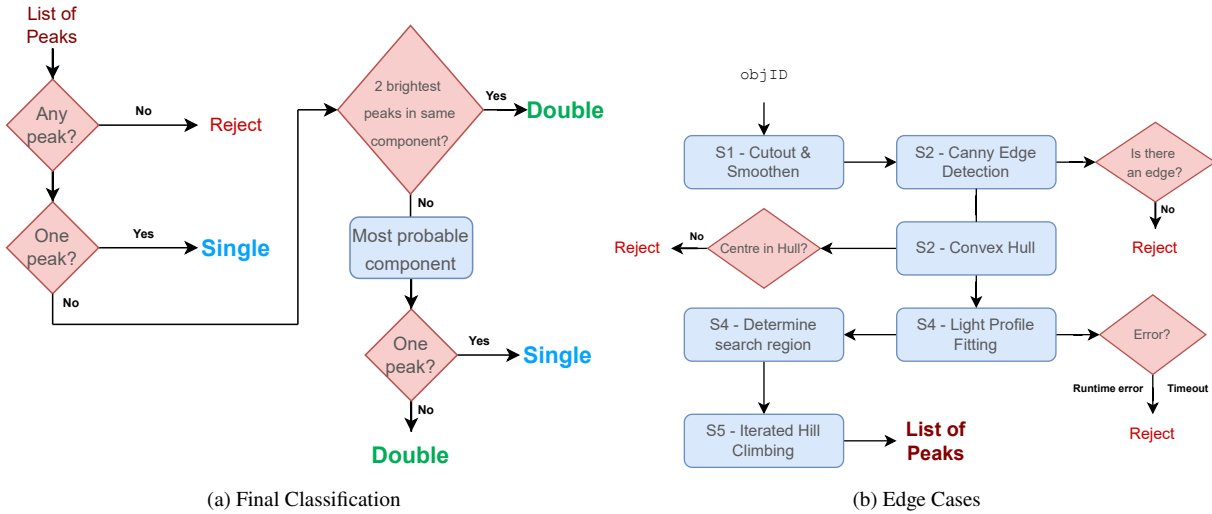
- *Subcase 3.2* - The connected component with the highest *chance* of representing a bonafide galaxy is selected. If it has one peak only, it is reported as a single nucleus. Otherwise, it is reported as double nuclei.

We justify each case of our classification criteria -

**Case 1** - It is possible that the Iterated Hill Climbing procedure returns no peak. This scenario can occur due to the first elimination criterion mentioned at the end of (Appendix Section A2).

**Case 2** - This represents a non ambiguous detection of a single nucleus galaxy.

**Case 3** - The detection of more than one peak requires careful analysis. If two or more peaks are detected, naively adjudging them as double nuclei would lead to excess false positive detections. **Figure 9b** is one such case where two peaks are detected, but they clearly belong to two distinct objects in the same field of view, and hence must be adjudged as a single nucleus galaxy. This *intuitive* notion of distinct objects is captured by the *mathematical* notion of connected components (Appendix Section A3). Moreover, it is not enough to simply report that a galaxy is single/double nuclei. We wish to know the exact coordinates of the peak(s) detected. Thus, in the case where  $\geq 2$  peaks are detected, it must be figured which two of the multiple


 Figure 10. Flowchart for *GOTHIC*

peaks faithfully represent a double nuclei galaxy. Figure 9a represents a scenario of multiple peaks in one connected component. In the general scenario, we would have multiple peaks detected in multiple connected components. To faithfully determine whether the galaxy is single/double nuclei, we require a notion of the *most probable* connected component that is likely to contain the peak(s) of interest (Appendix Section A3.1).

After the peaks have been located, we transform their pixel coordinates to (ra, dec) coordinates with the help of `astropy`. Figure 10a contains the classification procedure of Section 3.6 in a flowchart format.

### 3.7 Edge Cases in the Classification

Figure 10b shows the procedure of *GOTHIC* upto Iterated Hill Climbing (Section 3.5) with corresponding edge cases.

- (i) If the Canny procedure cannot detect edges, the galaxy is not amenable to further processing and hence rejected.
- (ii) We expect that the centre of the cutout would be inside the convex hull formed from the edges reported by Canny. If this is not the case, the object (*if any*) at the centre of the image is not bright enough for further processing, and subsequently rejected.
- (iii) On rare occasions, `scipy` throws errors while fitting the Sersic profile to the pixel histogram. In other cases, it can time out as well. Such samples are rejected.

## 4 EVALUATION OF THE EFFICIENCY OF *GOTHIC*

We show the peaks detected by *GOTHIC* on the representative examples in Figure 11. The final classification reported and peaks reported by *GOTHIC* agree well with the representative images in Figure 1 and Figure 2 and their descriptions in Table 1.

The two nuclei in the bona fide DNG examples (Rep 1 and Rep 2) are clearly identified. Rep 3 and Rep 7 showcase a star/galaxy in the line of sight of the central object respectively, and *GOTHIC* classifies both of them as a single galaxy. Rep 5 is a single nuclei galaxy with no object in its line of sight and is correctly classified as a single nuclei galaxy. Rep 6 is a star (*mislabeled as galaxy in SDSS*) and although it is reported to have one peak, it does not make a difference to our

final aim of searching for DNGs from a blind sample (Section 5). Rep 4 is a faint galaxy and *GOTHIC* does not detect any peaks in it, and hence has been rightly excluded from Figure 11.

We have also tested *GOTHIC* against the Gimeno Catalog and found a detection rate of  $\approx 90\%$ . The results of evaluating on the Gimeno Catalog can be found in Appendix Section B

## 5 APPLYING *GOTHIC* TO A SAMPLE OF ONE MILLION SDSS GALAXIES (I.E THE BLIND SAMPLE)

Given the high detection rate of *GOTHIC*, we applied it to a sample of 1,000,000 galaxies derived from SDSS DR16, including only those that had available spectroscopic data. We used images in the  $u, g, r, i$  bands and discarded the  $z$  band as we found images in this band to be often noisy.

For a randomly chosen galaxy, it is most probable that it is a single nuclei galaxy as DNGs are rare. Matching our expectations, we find 104,412 detections of DNGs reported by *GOTHIC* that represents a detection rate of  $\approx 10\%$ . There were a total 43,457 galaxies satisfying the edge-case criteria described Section 3.7 and hence discarded. Of these, 87 galaxies caused a run-time error in the light profile fitting procedure. The raw positive detections from *GOTHIC* may have false positives and these need to be filtered out. We applied the following sequence of conditions to arrive at a smaller sample, which is also amenable to visual analysis

- (i) The pixel coordinates of the detected nuclei need to be consistent across all the bands in which they are detected in. For example, if a peak is detected at  $(x, y)$  in the  $g$  band and *GOTHIC* reports a double detection in the  $r$  band, a corresponding peak has to be present in the  $r$  band within the  $3 \times 3$  window centred at  $(x, y)$ . If a given sample has a consistent detection of peaks across all bands in which *GOTHIC* reports a detection, we denote it as a *pure double*. Otherwise, we denote it as an *impure double*. We found 95, 159 pure doubles and used this subset for further filtration. The remaining 9,353 impure doubles are exempt from further study

- (ii) Although our initial one million sample had spectroscopic data available, it is not necessarily true that the DNG detected by *GOTHIC* always correspond to the galaxy referenced by its `obj_id`. *GOTHIC* is purely an image processing algorithm and is unaware

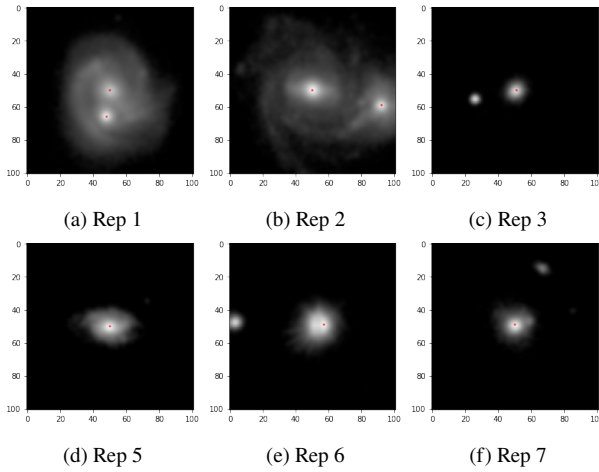


**Figure 11.** Final peaks after classification (marked as red pixel)

of the mapping between galaxies/peaks and `objID`s. Thus, we performed a coordinate to `objID` lookup of the DNGs detected by GOTHIC. We found that 47,521 of the 95,159 pure doubles have spectroscopic data available in SDSS.

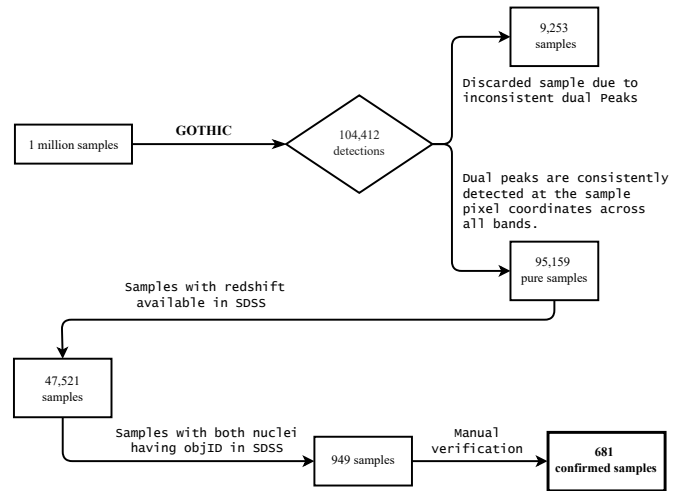
(iii) Of this filtered spectroscopic DNG sample, we choose only those DNGs that have distinct `objID`s corresponding to *both* the peaks of the DNGs. So from the 47,521 candidate DNGs, we obtained two groups of sources. The first was composed of 7,223 dual nuclei candidates where both nuclei were located within the SDSS fibre which has a diameter 3''. These sources could not be distinguished as two spectroscopic sources. We will follow up this sample in a later study using the spectral properties. This sample could be composed of close nuclei as well as single nuclei with outflows. The second group is a sample of 949 DNGs where both nuclei have spectroscopic ids. This sample is also amenable to manual analysis. This is a drastic reduction from the previous collection of 47,521 samples and arises from the imposed constraint of choosing *distinct* `objID` for the two peaks. GOTHIC is essentially an image processing algorithm and is unaware of whether a detected peak is a star, a starburst region of a galaxy, or a bona fide galactic nuclei. If SDSS catalogues distinct `objID`s at the location of the peaks, we gain additional confidence that GOTHIC has detected peaks that are highly likely to be galactic nuclei. This is precisely why we carry out further manual analysis on this sample; otherwise it would be contaminated with false positives. The sample simply happens to be small enough such that it can be analysed in its entirety.

Figure 12 shows a flowchart with the filtration steps. Appendix Figure B1 contains a panel of 48 representative DNGs after the filtration.

## 6 ANALYSIS OF THE REDUCED CANDIDATE SAMPLE

### 6.1 The final sample of galaxy nuclei pairs

As mentioned in the previous section, after applying GOTHIC to a sample of a million galaxies derived from SDSS DR16, we obtained two groups of sources. The first was composed of 7,223 dual nuclei candidates where both nuclei were located within the SDSS fibre which has a diameter 3''. These sources could not be distinguished as two spectroscopic sources and will be followed up in a later study using the spectral properties. This sample could be composed of close nuclei as well as single nuclei with outflows (Kharb et al. 2021).



**Figure 12.** Flowchart of Sample Filtration

The second sample was composed of 949 close galaxy nuclei pairs, where each nuclei had separate redshift identifications and object ids in SDSS DR16. In this paper we focus on this second sample of galaxy nuclei pairs that are very close in redshift ( $z$ ). The cutoff for  $\Delta z$  separation is defined by a distance ( $d$ ) which is taken to be approximately  $\Delta d < 40\text{kpc}$ , for all redshifts.

We visually checked the sample of 949 nuclei pairs to determine the success rate of GOTHIC. We found that **681** were actually true galaxy nuclei pairs, which gives a success rate of 71%. The false detection were mainly because of the following reasons. (i) The target galaxy did not have a compact bulge or nucleus and so GOTHIC incorrectly classified it as a merger (e.g. `objid` : 1237663239272923278). (ii) The companion galaxy did not have a redshift, even though it was classified as a spectroscopic source (e.g. `objid` : 1237671124306231474). (iii) The system appears to be a merger but the second galaxy does not have a clear nucleus (e.g. 1237658204507340929).

### 6.2 The redshift distribution of the initial and final samples

Figure 13a shows the redshift distribution of the initial sample of one million galaxies from SDSS DR16. The redshift extends from  $z=0$  to 0.832 and shows three peaks at approximately  $z=0.079, 0.353, 0.494$ . The redshift distribution of the confirmed dual nuclei (Figure 13b) is however slightly different and is distributed mainly between redshifts of  $z=0$  to 0.3. It shows only one peak at approximately  $z=0.073$ , which is close to the first peak of the one million galaxy distribution, but does not have the exact same value. A significant fraction of the 681 sources are classified as DAGN pairs using SDSS and their distribution is overlaid in pink. The DAGN have the same distribution as the nuclei pairs. The mean redshifts of the nuclei pairs and DAGN are very close to each other and are at  $z\approx 0.1$  as shown by the dashed vertical line in Figure 13b.

### 6.3 The classification of nuclei pairs using emission line ratios (BPT plot)

As described in the introduction our aim was to find a sample of DAGN (Rubinur et al. 2020) or triple AGN (Yadav et al. 2021). To obtain such samples, the SDSS class of the nuclei was very important. The SDSS classifies nuclei according to the emission

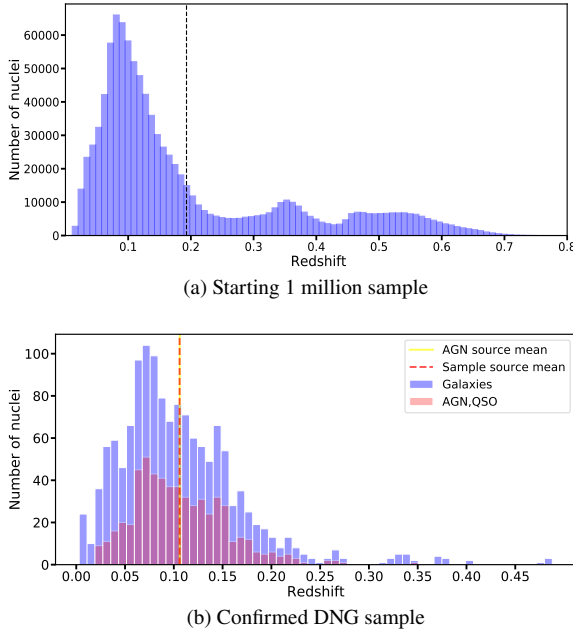


Figure 13. Redshift Distributions

lines in the spectra and the commonly used classes are starforming, starburst, AGN and QSO. If an AGN has broad components in the emission lines with doppler widths  $>200 \text{ kms}^{-1}$  it is classified as AGN broadline. The quasars (QSO), which are the most powerful AGN and have very broad emission lines, are identified using spectral templates.

In our sample of 949 nuclei pairs, 681 were visually confirmed to be nuclei pairs. We also found that many of the nuclei pairs in our sample are in small groups. This is not surprising as the clustering of galaxies has been known for decades (Dressler 1984). Using the SDSS class, we found that 11 nuclei pairs were DAGN, and either QSO-QSO or AGN-QSO pairs. The subclass of the nuclei were extracted from SDSS wherever it was available and this gave finally 45 DAGN. But we found that SDSS DR16 had tabulated the class and subclass for relatively few sources and hence this gave us a low number of DAGN which did not seem to be complete.

So for a better classification of the nuclei, we instead used the SDSS tabulated emission line data of the nuclei to plot the Baldwin, Phillips and Terlevich (BPT) diagram of our 681 dual nuclei sources. The BPT classifies nuclei based on the ratio of emission lines such as  $\text{H}\alpha$ ,  $[\text{OIII}]$ ,  $[\text{SII}]$ ,  $[\text{NII}]$ . Out of the total sample of 681 sources we have tried to incorporate the emission line data of all the nuclei for which data was available and obtained line data for 1393 nuclei (Figure 14). The classes of the nuclei are star forming (SF), composite, LINER and Seyfert. We have taken the solid curve in figure as the lower limit for finding an AGN and hence the classes composite, LINER and Seyfert are all considered to be AGN (Kauffmann et al. 2003). Studies have shown that the composite class does host AGN (Juneau et al. 2014).

However, there were some problems in obtaining the exact nature of some nuclei mainly because : (i) out of 1393 nuclei 14 had unavailable line emission data, (ii) 258 nuclei had either one of the emission line fluxes tabulated as negative or the denominator in the flux ratio was 0, (iii) 22 had negative emission line fluxes but the ratio was positive and (iv) one source had unusual  $[\text{OIII}]$  emission line values. So finally we could classify the nature of 1098 nuclei, of which 581 were AGN in nature and 517 were star forming. So the

Table 2. Frequency of each possible combination

combination	count
AGN-AGN	153
AGN-AGN-AGN	2
AGN-AGN-SF-SF	1
AGN-AGN-SF	3
AGN-SF	150
AGN-SF-SF	1
SF-SF	152
SF-SF-SF	2

final BPT plot had 1098 nuclei (Figure 14). We examined the nature of the sources in detail and found that 159 sources had at least two of the nuclei classified as AGN, so the number of dual AGN detected in our sample is 159 (Table 2). However, it must be noted that this is a lower limit, as the spectral information for several nuclei sources was not available. Of these 159 DAGN, 2 are in clusters of triple AGN lying with groups of 3 to 4 galaxies. Triple AGN are rare and only a few have been detected using X-ray and optical observations (Yadav et al. 2021). One DAGN is in a group of 4 nuclei with the other two being star forming in nature. One DAGN is in a triplet system where the third is a star forming nucleus.

The frequency of the different combinations obtained is given in Table 2. It is clear that the number of AGN-SF and DAGN are comparable. This is surprising as the number of star forming nuclei is generally found to be larger than the number of DAGN in previous studies (e.g. Rubinur et al. (2019)). But our sample is composed of relatively close nuclei pairs, hence this suggests that star formation maybe quenched in galaxies as the nuclei come closer during mergers. Table 2 also shows that the number of composite class nuclei is relatively large. These nuclei have star formation associated with AGN activity and may represent galaxies evolving from starburst dominated galaxies to AGN dominated ones (Yuan et al. 2010). The number of star forming (SF-SF) or AGN-SF pairs is also very large, implying that star formation is an integral part of the interaction process, but may not be the dominant one as the number of SF-SF nuclei and DAGN are comparable.

#### 6.4 The color magnitude plot of the galaxy nuclei pairs and comparison with the general population of SDSS galaxies

The color magnitude diagram (CMD) of galaxies is usually a plot of the color of galaxies (e.g.  $(u-r)$  magnitudes) against their absolute R band magnitude ( $M_R$ ) and is known to show a bimodal distribution (Bell et al. 2004). The  $(u-r)$  color represents the star formation rate (SFR) per unit stellar mass whereas  $M_R$  represents the stellar mass of a galaxy. The CMD is bimodal with the star forming galaxies lying in the bluer and hence lower part of the CMD whereas the redder galaxies with low SFRs are in the upper part of the CMD (Schawinski et al. 2014). These two regions are traditionally called the blue cloud and red sequence respectively, although other wavebands colors such as  $(NUV-r)$  have been also used (Salim et al. 2007).

Figure 15 shows the CMD of all the galaxies from the 681 galaxies, including galaxies in pairs of small groups. The total number is 1393. A comparison sample of 996051 SDSS galaxies at redshifts  $z < 0.760$  are plotted in grey scale. The integrated  $(u-r)$  colours of the galaxies are plotted against their absolute magnitudes in the r band  $M_R$  after they were corrected for Galactic extinction. Galaxies belonging to group having different number of companions are given different color (red for galaxies in group having 2 galaxies, blue for galaxies in groups of 3 galaxies, black for groups of 4 galaxies) and are shown

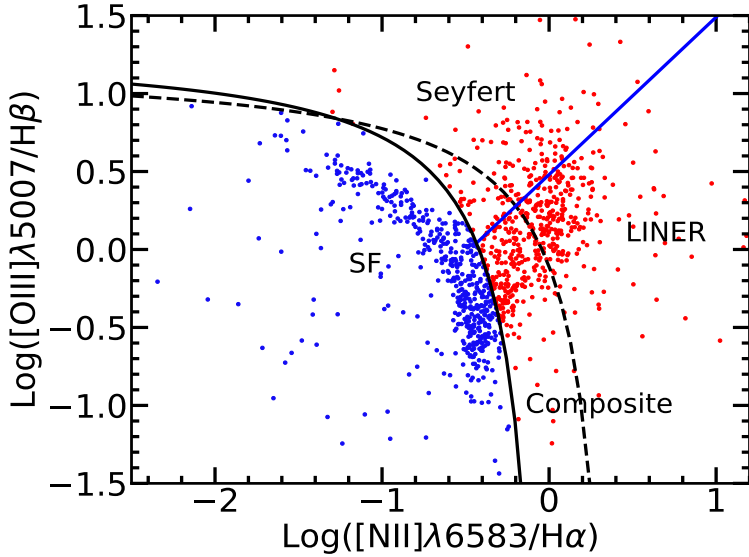


**Figure 14.** The BPT Diagram of the emission line data of 1098 nuclei that lie in pairs or small groups i.e. they are derived from the sample of 681 DNG. From the position of the nuclei, their nature could be explained with reference to classification curves: The black solid line is the curve fit signifying the lower limit for AGNs (Kauffmann et al. 2003), hence the region below this curve is considered SF. The black dashed curve is the upper limit for star burst (Kewley et al. 2006), sources in region between the solid black curve and dashed black curve are considered composite. The solid blue line separated LINER from seyferts (Fernandes et al. 2010)

The distribution obtained is as follows : SF=528, composite=246, LINER=228 and Seyfert=118

as individual coloured points superimposed on a grey-scale contour map. It is interesting to see that a large fraction of the dual nuclei galaxies lie in the redder part of the CMD. This suggests that the star formation associated with the merging process is quenched as the nuclei come closer. The galaxies also have absolute magnitudes  $M_R < 18$  which suggests that the dual nuclei are associated with relatively more massive galaxies.

To examine this in more details we plotted the galaxy nuclei according to their type in Figure 16 (Figure 16a, Figure 16b, Figure 16c). It is clear that the SF nuclei extend over a relatively larger range of colors with a significant fraction lying in the blue region of the CMD. But as we move from SF-SF pairs to AGN-SF pairs and then finally to DAGN, the colors become redder with the DAGN nuclei lying towards the reddest part of the CMD.

## 7 DISCUSSION

In this study we have discovered a new sample of dual and triple AGN, apart from mixed AGN-star forming nuclei pairs. We have used a code to automatically find the initial sample of dual nuclei and confirmed their nature using empirical relations such as those used in the BPT plot. This code called GOTHIC can be used to determine samples of galaxy merger remnants in other optical or multiwavelength datasets. Such methods are important for finding SMBH pairs in large data sets (Mannucci et al. 2022). The samples of DAGN are important inputs for models that predict the gravitation wave background from SMBH binaries (Casey-Clyde et al. 2022).

One of the main outcomes of this study is that dual AGN are not as common as predicted by simulation studies (Volonteri et al. 2022; Bhowmick et al. 2020). We have used a million galaxies in SDSS for our automated detection of galaxy pairs, but the number that we obtained is quite small ( 681). The GOTHIC code selects galaxy pairs within a box size of  $40'' \times 40''$ . Since the redshift distribution extends from  $z=0$  to 0.7, this translates approximately to a typical

projected separation of a few kpc at  $z=0$  to a maximum of  $10''$  or 145kpc at  $z=0.7$  (where  $H_0 = 70 \text{ km s}^{-1} \text{ Mpc}^{-1}$ ). The number of dual AGN is 159, of which two are triple AGN. These numbers however, are lower limits, since we had to exclude nuclei pairs that lie within the SDSS fibre radius of  $1.5''$  as well as those that did not have good S/N spectroscopic data and so reliable emission line ratios could not be obtained. But overall these numbers suggest that dual and multiple AGN systems are not common (Table 2). The DAGN reported in the literature (Das et al. 2018) are often serendipitous in nature, and multiwavelength surveys usually do not yield many dual AGN (Rubinur et al. 2019). But AGN are known to produce winds/outflows that are important for building up the hot gas halos or circum-galactic medium (CGM) around galaxies and the presence of dual AGN would increase this effect. Since the numbers of DAGN detected are relatively low, our results suggest that the starburst winds/outflows in galaxy mergers, and not just the dual AGN, maybe be important for the growth of CGM around galaxies.

Another interesting implication of our study is that the dual nuclei galaxies and the dual AGN lie in the red cloud of the galaxy color magnitude plot (Figure 14). This suggests that as the nuclei come closer during mergers the star formation is quenched. This has been observed in ultraluminous galaxies (ULIRGs) that are the results of gas rich major mergers and appear to be evolving into elliptical galaxies (Dasyra et al. 2006) and in some case radio galaxies as well (Nandi et al. 2021). Figure 16 shows the color magnitude diagram (CMD) for the different dual nuclei pairs, star forming (SF-SF), mixed (AGN-SF) and DAGN. The SF-SF pairs lie over a wide range of colors (g-r) whereas the DAGN are mainly found in the red region of the CMD. This suggests that the AGN activity in DAGN is quenching star formation.

The DAGN are also more massive systems compared to the SF-SF and AGN-SF pairs. This indicates that the formation of the DAGN is the final stage in evolution of galaxy mergers and their nuclei. However, to understand this in more detail, the parameters of the

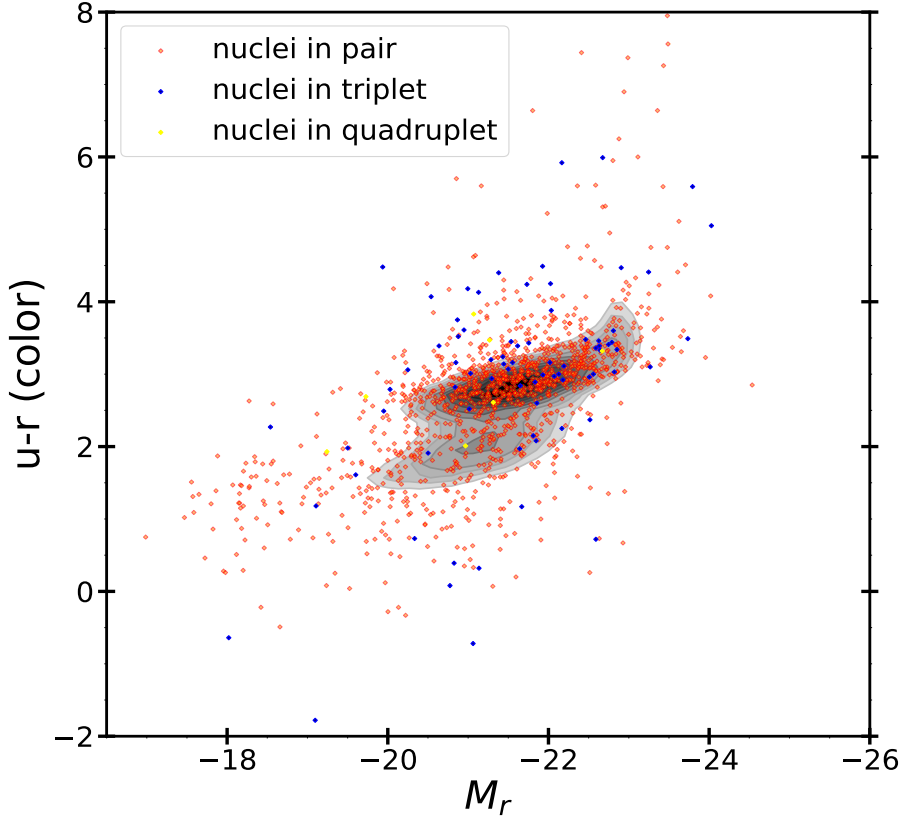


**Figure 15.** The color magnitude diagram (CMD) of all 1393 galaxies in pairs of small groups (i.e. the total number of sources from the 681 galaxies in pairs and including their companions; a few are in groups of 3 or 4). This was derived visually from the sample derived using the GOTHIC algorithm on a sample of 1 million galaxies (of which 21 galaxies had insufficient data). A comparison sample of 907844 SDSS galaxies at redshifts  $z < 0.5$  are plotted in grey scale. The integrated  $(u - r)$  colours corrected for extinction of the galaxies are plotted against their absolute magnitudes in the  $r$  band,  $M_r$ . Galaxies belonging to group having different number of companions are given different color (red for galaxies in group having 2 galaxies, blue for galaxies in group having 3 galaxies, yellow for galaxies in group having 4 galaxies) and are shown as individual coloured points superimposed on a grey-scale contour map of the distribution of the comparison sample, where the darker shades represent the denser regions. The density contour levels are in units of the number of galaxies per grid unit of size 0.10 mag in  $M_r$  and 0.155 mag in  $(u - r)$ : 2000, 2500, 3000, 3500, 4200, 4800, 5400, 6000, 6600, 7200, 8000, 8485.

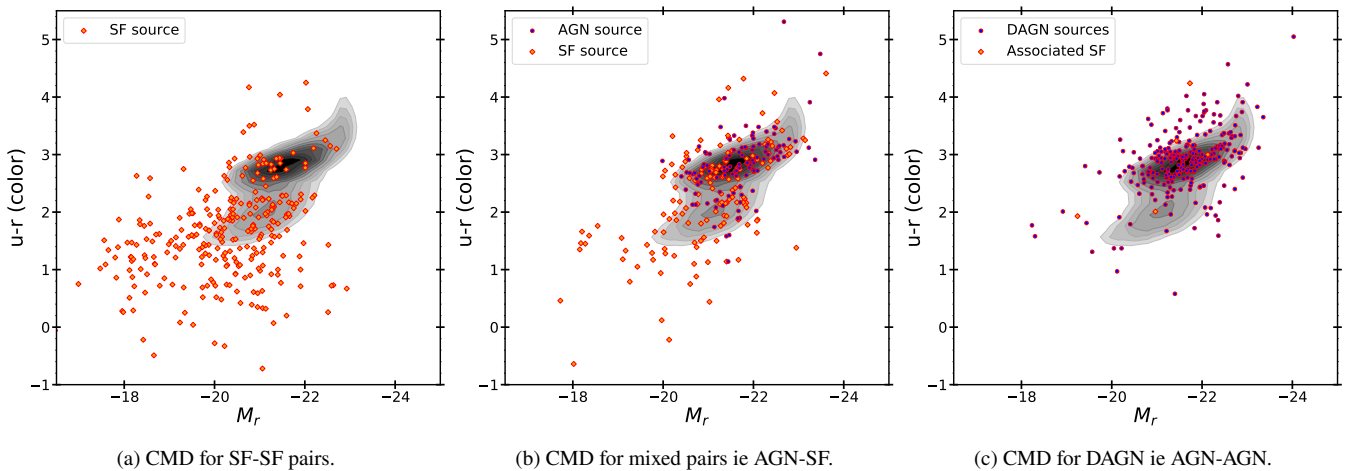


**Figure 16.** The 3 plots from left to right (a, b, c) show the relative positions of the star forming nuclei pairs (SF-SF), the mixed AGN-SF pairs and the DAGN on the CMD. The DAGN includes the two triple AGN.

nuclei, their separation and SMBH masses need to be determined. It will also be interesting to see how the DAGN evolve in cosmological simulations and if they show similar trends in the CMD. These questions will be followed up in our subsequent paper.

## 8 CONCLUSION

We present a novel detection algorithm called *GOTHIC*, that detects close nuclei pairs in given galaxy images from SDSS DR16. Our aim is to obtain a sample double nuclei galaxies and detect dual AGN (DAGN). The algorithm has been tested on an existing catalog galaxy pairs that host double nuclei, and the results show a detection rate of  $\approx 90\%$ . Subsequently, we applied *GOTHIC* on an *unknown* sample of one million galaxies that have spectroscopic data in SDSS DR16. From this sample 100,000 galaxies were reported to be double-nuclei by *GOTHIC*. After careful filtration of the detected sample and removal of likely false detections, a small subset of 949 galaxies was studied visually to produce a confirmed sample of dual nuclei systems. We detected 681 nuclei pairs, and then used their emission line fluxes to determine their positions (AGN or star forming) on the BPT plot. The BPT showed that 159 are DAGN, of which 2 are triple AGN systems. The others are either star forming pairs (SF-SF) or AGN-star forming (AGN-SF) pairs. The color magnitude plot of the different nuclei pairs shows that the DAGN usually lie in galaxies that are redder and more massive compared to the SF-SF and AGN-SF pairs. Our results also suggest that DAGN may play a role in quenching star formation in galaxy mergers.

## ACKNOWLEDGEMENTS

The first author gratefully acknowledges the support received from the Indian Institute of Astrophysics, Bangalore, India during an internship. Second author acknowledges the support of the Indian Institute of Astrophysics, Bangalore, India. M.Das acknowledges the support of the Science and Engineering Research Board (SERB) MATRICS grant MTR/2020/000266 for this research. S.Saha would like to thank the Science and Engineering research Board (SERB), Department of Science and Technology, Government of India, for supporting our research by providing us with resources to conduct our study. The project reference number is EMR/2016/005687.

Funding for the SDSS and SDSS-II has been provided by the Alfred P. Sloan Foundation, the Participating Institutions, the National Science Foundation, the U.S. Department of Energy, the National Aeronautics and Space Administration, the Japanese Monbukagakusho, the Max Planck Society, and the Higher Education Funding Council for England. The SDSS Web Site is <http://www.sdss.org/>. The SDSS is managed by the Astrophysical Research Consortium for the Participating Institutions. The Participating Institutions are the American Museum of Natural History, Astrophysical Institute Potsdam, University of Basel, University of Cambridge, Case Western Reserve University, University of Chicago, Drexel University, Fermilab, the Institute for Advanced Study, the Japan Participation Group, Johns Hopkins University, the Joint Institute for Nuclear Astrophysics, the Kavli Institute for Particle Astrophysics and Cosmology, the Korean Scientist Group, the Chinese Academy of Sciences (LAMOST), Los Alamos National Laboratory, the Max-Planck- Institute for Astronomy (MPIA), the Max-Planck-Institute for Astrophysics

(MPA), New Mexico State University, Ohio State University, University of Pittsburgh, University of Portsmouth, Princeton University, the United States Naval Observatory, and the University of Washington.

## REFERENCES

Aggarwal K., et al., 2019, *ApJ*, **880**, 116  
 Barton E. J., Geller M. J., Kenyon S. J., 2000, *ApJ*, **530**, 660  
 Bell E. F., et al., 2004, *ApJ*, **608**, 752  
 Bellovary J. M., Governato F., Quinn T. R., Wadsley J., Shen S., Volonteri M., 2010, *ApJ*, **721**, L148  
 Bhattacharya A., Saha S., Das M., 2020, GOTHIC: Double nuclei galaxy detector (ascl:2011.008)  
 Bhowmick A. K., Di Matteo T., Myers A. D., 2020, *MNRAS*, **492**, 5620  
 Bickley R. W., et al., 2021, *Monthly Notices of the Royal Astronomical Society*, **504**, 372–392  
 Blumenthal K. A., et al., 2019, *Monthly Notices of the Royal Astronomical Society*, **492**, 2075  
 Bottrell C., et al., 2019, *Monthly Notices of the Royal Astronomical Society*, **490**, 5390  
 Bottrell C., Hani M. H., Teimoorinia H., Patton D. R., Ellison S. L., 2021, *MNRAS*,  
 Bustamante S., Ellison S. L., Patton D. R., Sparre M., 2020, *MNRAS*, **494**, 3469  
 Canny J., 1986, *IEEE Transactions on Pattern Analysis and Machine Intelligence*, PAMI-8, 679  
 Caon N., Capaccioli M., D’Onofrio M., 1993, *Monthly Notices of the Royal Astronomical Society*, **265**, 1013  
 Capelo P. R., Dotti M., Volonteri M., Mayer L., Bellovary J. M., Shen S., 2017, *MNRAS*, **469**, 4437  
 Casey-Clyde J. A., Mingarelli C. M. F., Greene J. E., Pardo K., Nañez M., Goulding A. D., 2022, *ApJ*, **924**, 93  
 Cormen T. H., Leiserson C. E., Rivest R. L., Stein C., 2009, *Introduction to Algorithms*, Third Edition, 3rd edn. The MIT Press  
 Das M., Rubinur K., Kharb P., Varghese A., Novakkuni N., James A., 2018, *Bulletin de la Societe Royale des Sciences de Liege*, **87**, 299  
 Dasyra K. M., et al., 2006, *ApJ*, **651**, 835  
 Davies J. J., Crain R. A., Oppenheimer B. D., Schaye J., 2020, *MNRAS*, **491**, 4462  
 De Rosa A., et al., 2019, *New Astron. Rev.*, **86**, 101525  
 Dressler A., 1984, *ARA&A*, **22**, 185  
 Ekici C., Kocayusufoglu I., Akca Z., 1998, *Turkish Journal of Mathematics*, **22**, 295  
 Ellison S. L., Patton D. R., Simard L., McConnachie A. W., Baldry I. K., Mendel J. T., 2010, *MNRAS*, **407**, 1514  
 Fernandes R. C., Stasińska G., Schlickmann M. S., Mateus A., Asari N. V., Schoenell W., Sodré L. J., (the SEAGal collaboration) 2010, *Monthly Notices of the Royal Astronomical Society*, **403**, 1036  
 Fielding D. B., et al., 2020, *ApJ*, **903**, 32  
 Gimeno G. N., Díaz R. J., Carranza G. J., 2004, *The Astronomical Journal*, **128**, 62  
 Goulding A. D., Pardo K., Greene J. E., Mingarelli C. M. F., Nyland K., Strauss M. A., 2019, *ApJ*, **879**, L21  
 Greene J. E., et al., 2021, *ApJ*, **917**, 17  
 Hopkins P. F., Kocevski D. D., Bundy K., 2014, *Monthly Notices of the Royal Astronomical Society*, **445**, 823  
 Juneau S., et al., 2014, *ApJ*, **788**, 88  
 Kauffmann G., et al., 2003, *Monthly Notices of the Royal Astronomical Society*, **346**, 1055  
 Kewley L. J., Groves B., Kauffmann G., Heckman T., 2006, *Monthly Notices of the Royal Astronomical Society*, **372**, 961  
 Kharb P., Lal D. V., Merritt D., 2017a, *Nature Astronomy*, **1**, 727  
 Kharb P., Subramanian S., Vaddi S., Das M., Paragi Z., 2017b, *ApJ*, **846**, 12  
 Kharb P., Subramanian S., Das M., Vaddi S., Paragi Z., 2021, *ApJ*, **919**, 108  
 Kim E., et al., 2021, *MNRAS*, **507**, 3113

Komossa S., Burwitz V., Hasinger G., Predehl P., Kaastra J. S., Ikebe Y., 2003, *ApJ*, **582**, L15

Koss M., Mushotzky R., Veilleux S., Vasudevan R., Miller N., Sanders D. B., Schawinski K., Trippe M., 2011, *The Astrophysical Journal*, **735**, L42

Koss M., Mushotzky R., Treister E., Veilleux S., Vasudevan R., Trippe M., 2012, *The Astrophysical Journal*, **746**, L22

Makhija S., Saha S., Basak S., Das M., 2019, *Astronomy and Computing*, **29**, 100313

Mannucci F., et al., 2022, arXiv e-prints, p. [arXiv:2203.11234](https://arxiv.org/abs/2203.11234)

Maschmann D., Melchior A.-L., Mamon G. A., Chilingarian I. V., Katkov I. Y., 2020, *A&A*, **641**, A171

Mazzarella J. M., et al., 2012, *AJ*, **144**, 125

Mezcua M., Lobanov A. P., Mediavilla E., Karouzos M., 2014, *The Astrophysical Journal*, **784**, 16

Nandi S., Das M., Dwarakanath K. S., 2021, *MNRAS*, **503**, 5746

Nelson D., et al., 2021, The IllustrisTNG Simulations: Public Data Release ([arXiv:1812.05609](https://arxiv.org/abs/1812.05609))

Nevin R., Blecha L., Comerford J., Greene J., 2019, *The Astrophysical Journal*, **872**, 76

Patton D. R., Atfield J. E., 2008, *ApJ*, **685**, 235

Patton D. R., Qamar F. D., Ellison S. L., Bluck A. F. L., Simard L., Mendel J. T., Moreno J., Torrey P., 2016, *MNRAS*, **461**, 2589

Patton D. R., et al., 2020, *MNRAS*, **494**, 4969

Peterson B. M., 1997, An Introduction to Active Galactic Nuclei. Cambridge University Press

Price-Whelan A. M., et al., 2018, *The Astronomical Journal*, **156**, 123

Reines A. E., Condon J. J., Darling J., Greene J. E., 2020, *ApJ*, **888**, 36

Ricarte A., Tremmel M., Natarajan P., Zimmer C., Quinn T., 2021, *MNRAS*, **503**, 6098

Rodriguez C., Taylor G. B., Zavala R. T., Peck A. B., Pollack L. K., Romani R. W., 2006, *ApJ*, **646**, 49

Rubinur K., Das M., Kharb P., 2018, *Journal of Astrophysics and Astronomy*, **39**, 8

Rubinur K., Das M., Kharb P., 2019, *MNRAS*, **484**, 4933

Rubinur K., Kharb P., Das M., Rahna P. T., Honey M., Paswan A., Vaddi S., Murthy J., 2020, *MNRAS*,

Salim S., et al., 2007, *ApJS*, **173**, 267

Sanders D. B., Mirabel I. F., 1996, *ARA&A*, **34**, 749

Schawinski K., et al., 2014, *MNRAS*, **440**, 889

Sérsic J. L., 1963, Boletín de la Asociación Argentina de Astronomía La Plata Argentina, **6**, 41

Shannon R. M., et al., 2015, *Science*, **349**, 1522

Shlosman I., Begelman M. C., Frank J., 1990, *Nature*, **345**, 679

Sklansky J., 1982, *Pattern Recognition Letters*, **1**, 79

Stemo A., Comerford J. M., Barrows R. S., Stern D., Assef R. J., Griffith R. L., Schechter A., 2021, *ApJ*, **923**, 36

Talvila E., Wiersma M., 2012, Simple derivation of basic quadrature formulas ([arXiv:1202.0249](https://arxiv.org/abs/1202.0249))

Thomas D., Maraston C., Bender R., Mendes de Oliveira C., 2005, *ApJ*, **621**, 673

Tubín D., et al., 2021, *The Astrophysical Journal*, **911**, 100

Vincent O. R., Folorunso O., 2009, in in proceedings of Informing Science & IT Education Conference (InSITE).

Virtanen P., et al., 2020, *Nature Methods*, **17**, 261

Volonteri M., Pfister H., Beckmann R., Dotti M., Dubois Y., Massonneau W., Musoke G., Tremmel M., 2022, *MNRAS*, **514**, 640

White S. D. M., Rees M. J., 1978, *MNRAS*, **183**, 341

Yadav J., Das M., Barway S., Combes F., 2021, *A&A*, **651**, L9

Yuan T. T., Kewley L. J., Sanders D. B., 2010, *ApJ*, **709**, 884

Zhou H., Wang T., Zhang X., Dong X., Li C., 2004, *ApJ*, **604**, L33

## APPENDIX A: DETAILS OF SELECTED ALGORITHMS

### A1 Radius to Frequency Relation

The Sersic profile is traditionally stated in terms of the radius from the galactic centre (eq 1). However, this information is not readily calculable and moreover, it is unsuitable for fitting to the data available at hand *i.e.*, the image histogram. As a simple heuristic, we use the taxicab norm [Ekici et al. \(1998\)](#) of the pixel coordinates to represent the radial distance from the galactic centre.

Formally stated, in the 2-D cartesian plane with  $(0, 0)$  as the origin, the "radial" distance of the point  $(x, y)$  in pixel coordinate is  $|x| + |y|$ . In order to translate the radius  $R$  (which appears as the independent variable in the Sersic equation) into frequency  $f$ , we need to find the set of points  $\mathcal{S}_R = \{(x, y) : |x| + |y| = R\}$ . We define the cardinality of this set is the frequency *i.e.*,  $f = |\mathcal{S}_R|$ .

Denote  $f(R)$  as the number of points that the locus of  $|x| + |y| = R$  passes through. By closely observing the red and blue lines, it can be seen that the following recurrence holds

$$f(R + 1) = f(R) + 4 \quad (\text{A1})$$

With the base case of  $f(1) = 4$ , we obtain

$$f(R) = 4R \quad (\text{A2})$$

### A2 Hill Climbing

#### HILL-CLIMB( $pt, reg, img$ )

```

1 newpt  $\leftarrow$  NULL
2 while  $pt \neq newpt$ 
3   do  $neighs \leftarrow$  GET-NEIGHBORS( $pt, 3, reg$ )
4    $newpt \leftarrow pt$ 
5   for  $n$  in  $neighs$ 
6     do if  $img[n.x, n.y] > img[newpt.x, newpt.y]$ 
7    $pt \leftarrow newpt$ 
8 return  $newpt$ 
```

The formal hill climbing algorithm is given in algorithm A2. It takes as its argument the randomly initialized starting point  $pt$ .  $reg$  is list  $\{(x, y)\}$  of pixel coordinates that represents the search region for peak finding (*for example, the red region in figure 7a*). Finally, the variable  $img$  is a dictionary that maps coordinates  $(x, y)$  of the smoothed image to its corresponding pixel value (*between 1 and 255 for grayscale images*). **NULL** represents a dummy value used for initialization.

The procedure **GET-NEIGHBORS** returns a list of pixels upto the nearest 3<sup>rd</sup> neighbors (*in terms of the supremum norm*) of the input point  $pt$ . These neighbors form a  $7 \times 7$  box at the centre of which lies the point  $pt$ . Variable  $reg$  is also required by the procedure so that it can exclude any point in the  $7 \times 7$  box that may lie outside the search (*red*) region.

Semantically, the variable  $newpt$  represents the coordinate that has the highest pixel value in comparison to the current  $pt$ . Its value is determined by lines 4 to 7 by iterative comparison of pixel values with each of the neighbors of  $pt$  using the image dictionary  $img$ . If no higher neighbor is found, we obtain the condition  $pt = newpt$ . This is to be interpreted as — *no higher neighbor of pt was found, so it must be a peak*. Finally, the while loop exits due to the guard condition in line 2 and it is returned in line 9.

It is possible to consider only the 1<sup>st</sup> or 2<sup>nd</sup> nearest neighbors when performing the neighbor search, however, it leads to a longer trail between the initial point and the final peak due to smaller discrete steps. This results in a slowdown of the HILL-CLIMB procedure.

For optimal performance, we consider 3<sup>rd</sup> neighbors only. Using higher-order neighbors such as 4, 5 may lead to false negatives in the scenarios where the DNG peaks are in close proximity *i.e.*, the highest peak would always be chosen if it happens to be a close neighbor of the second highest peak. Hence, it could be mistakenly reported as a single-nucleus galaxy.

#### ITERATED-HILL-CLIMB( $reg, img$ )

```

1 peak_list  $\leftarrow \Phi$ 
2  $i \leftarrow 0$ 
3 repeat  $pt \leftarrow$  CHOOSE-RANDOM( $reg$ )
4    $peak \leftarrow$  HILL-CLIMB( $pt, reg, img$ )
5    $c_1 \leftarrow peak$  not in  $peak_list$ 
6    $c_2 \leftarrow$  SNR( $peak$ )  $\geq 3$ 
7    $neighs \leftarrow$  GET-NEIGHBORS( $pt, 3, reg$ )
8    $c_3 \leftarrow$  INTERSECTION( $neighs, peak_list$ ) is  $\Phi$ 
9   if  $c_1$  and  $c_2$  and  $c_3$ 
10    then APPEND( $peak, peak_list$ )
11     $i \leftarrow i + 1$ 
12 until  $i = 1,000$ 
13 return  $peak_list$ 
```

Algorithm A2 is the iterated hill climbing algorithm that is used to find the list of candidate peaks. It takes as input the search region  $reg$  and the image dictionary  $img$ . Line 1 initializes the variable  $peak_list$  to the empty list  $\Phi$  and the counter  $i$  is set to 0 in line 2.

It first chooses a random point in the search region via procedure **CHOOSE-RANDOM** at line 3, and it is subsequently passed to the hill-climbing subroutine in line 4. After a peak has been found, it is subjected to the following elimination conditions to decide if it should be included in  $peak_list$

- (i) The SNR at the peak must be greater than 3 standard deviations
- (ii) The peak should not already exist in the list of peaks
- (iii) No neighboring pixel (*upto the nearest third*) must already exist in the list of peaks — This condition has been included because **HILL-CLIMB** uses neighbors upto the nearest third in finding the highest neighboring pixel. Hence, it does not make sense to have two peaks in the peak list that are atmost third neighbors apart. This scenario is only relevant when any two peaks are equal in pixel value and happen to lie in each others' neighborhoods.

Only if the above three conditions are satisfied is the new peak appended to the list in line 10. Finally, the peak list is returned after 1,000 iterations are concluded. It is precisely this peak list that has been marked in red in figures 8a and 8b respectively.

### A3 Connected Components

Simply stated, the number of connected components is the number disjoint portions of the search region of a galaxy. For example, there is 1 connected component in Rep 5 (figure 7a) and 2 connected components in Rep 7 (figure 7b). The algorithm for computing disjoint regions is a standard one and can be easily referenced in [Cormen et al. \(2009\)](#).

The astute viewer may point out that Rep 5 (7a) actually contains 2 connected components and that Rep 7 (7b) contains 3 connected components. Although it is true, these components are too small in size to represent any astronomical object (*star or galaxy*) in SDSS. It is an artefact of the noise in the image. Hence, all components that are *smaller* than a certain threshold size are ignored.

### A3.1 Most Probable Component

When there are multiple peaks dispersed across multiple components, it is crucial to identify which component contains our peak(s) of interest. In a nutshell, a component  $C$  is a set of pixel coordinates  $C = \{(x, y)\}$ . The number of pixels in a component would be the cardinality,  $|C|$ . The search region for an image can be typically broken down into  $n$  components as  $\{C_1, C_2, \dots, C_n\}$ . One of these components contains our peak of interest, denote it by  $C_p$ . We describe intuitively the expected characteristics of such a  $C_p$  with the following heuristics.

(i) The component must be close to the centre of the image. This is intuitive as we take a cutout centred at the coordinates of an object.

(ii) The component must have a higher cardinality than other components. This ought to be true in most cases as other stray objects on the line of sight of the cutout are expected to be smaller in size.

It would be incorrect to choose a component that has higher cardinality but is distant from the centre of the image as it is more likely to represent a stray object on the line of sight. Hence heuristic (i) above must be given higher priority than (ii).

To capture these notions into a mathematical formulation, we define the *midpoint* of a component as the average of its constituent pixel coordinates *i.e.*,  $m_C = \left( \frac{\sum x}{|C|}, \frac{\sum y}{|C|} \right)$  for  $(x, y) \in C$ . Subsequently, the *distance* of component is its 2-D pixel distance from the centre of the image,  $p$ . Mathematically, the distance of a component is  $d_C = \sqrt{(m_{Cx} - p_x)^2 + (m_{Cy} - p_y)^2}$ .

**Step 1** - We aggregate the components into bins of 10 units of pixel distance. For example, all components with their distance  $0 \leq d_C < 10$  would be put in the first bin,  $10 \leq d_C < 20$  would be put in the second bin and so on. After the binning process, we consider only the first bin,  $\mathcal{B}_1$ , as all its constituent components are closest to the centre of the image. This captures heuristic (i).

**Step 2** - We sort the constituents of  $\mathcal{B}_1$  in descending order of their cardinality. Finally, we set the most probable component  $C_p$  as the first element of  $\mathcal{B}_1$ , which would be the largest component. This captures heuristic (ii).

This two step procedure gives more priority to heuristic (i) than (ii) because the binning procedure eliminates components that are distant from the centre. The large component from only the *first* bin is chosen.

### APPENDIX B: CHECKING GOTHIC AGAINST THE GIMENO CATALOG

We use the Gimeno Catalog as a test sample to check *GOTHIC* against. Of the subset which had imaging data available in SDSS DR8 [Mezcua et al. \(2014\)](#), we found that 47 objects were listed in SDSS DR16. We let the algorithm run on this sample and found a detection rate of 89.36%. The output provided by *GOTHIC* is listed in table B1. There are 5 objects that *GOTHIC* was not able to successfully identify. On visual observation, it was found that except 1237680245191868529, the non-identified objects represent a galaxy with a bright star directly on the same line of sight which prevents *GOTHIC* from working.

**Table B1.** Results of *GOTHIC* on the Gimeno Catalog

objID	Peak 1	Peak 2
1237678661428314227	(50, 50)	(56, 41)
1237651737370296329	(50, 51)	(36, 63)
1237661433243828392	(61, 51)	(50, 50)
1237680265075884063	-	-
1237678622230773769	(50, 50)	(69, 56)
1237663530798219364	(50, 49)	(38, 37)
1237680332175769723	(49, 50)	(57, 40)
1237661950781685800	(51, 32)	(50, 50)
1237668670253564040	(50, 50)	(45, 39)
1237661850396327969	(50, 50)	(21, 50)
1237680286536826907	(49, 50)	(1, 33)
1237658801497178131	(50, 50)	(43, 42)
1237679436129632275	(50, 50)	(50, 58)
1237661816027938877	(41, 44)	(50, 51)
1237655463774191765	(93, 24)	(50, 49)
1237680529207066652	(50, 50)	(50, 62)
1237665329853562899	(57, 24)	(50, 49)
1237661063879000073	(50, 50)	(69, 69)
1237658204517171275	(50, 50)	(44, 25)
1237679456529743995	(56, 58)	(46, 42)
1237664289930346555	(53, 62)	(50, 48)
1237661950783979531	(50, 50)	(60, 60)
1237680271501426770	(50, 50)	(48, 37)
1237661358620082187	(50, 50)	(57, 57)
1237653612113166459	(50, 50)	(61, 53)
1237651539239895057	(51, 50)	(45, 59)
1237657589780512816	(50, 50)	(43, 42)
1237654400761790563	(50, 50)	(59, 55)
1237650761852846175	(50, 50)	(68, 59)
1237654382516699209	(49, 50)	(49, 36)
1237655472898637896	(50, 50)	(52, 40)
1237670961092558855	(50, 50)	(28, 16)
1237657856073269409	(50, 50)	(59, 27)
1237670961628971177	-	-
1237666300016591063	(50, 50)	(66, 59)
1237655463772618940	(50, 50)	(34, 55)
1237665569292943466	(50, 50)	(41, 49)
1237661977085018198	(50, 50)	(68, 40)
1237678598094454843	(50, 50)	(49, 45)
1237657771786960904	(45, 59)	(50, 50)
1237664871897038979	(50, 50)	(52, 40)
1237679581622698224	-	-
1237654640211656710	-	-
1237680245191868529	-	-
1237658491207680027	(74, 68)	(48, 51)
1237666301638279613	(50, 50)	(59, 92)
1237667734504407135	(54, 56)	(39, 59)

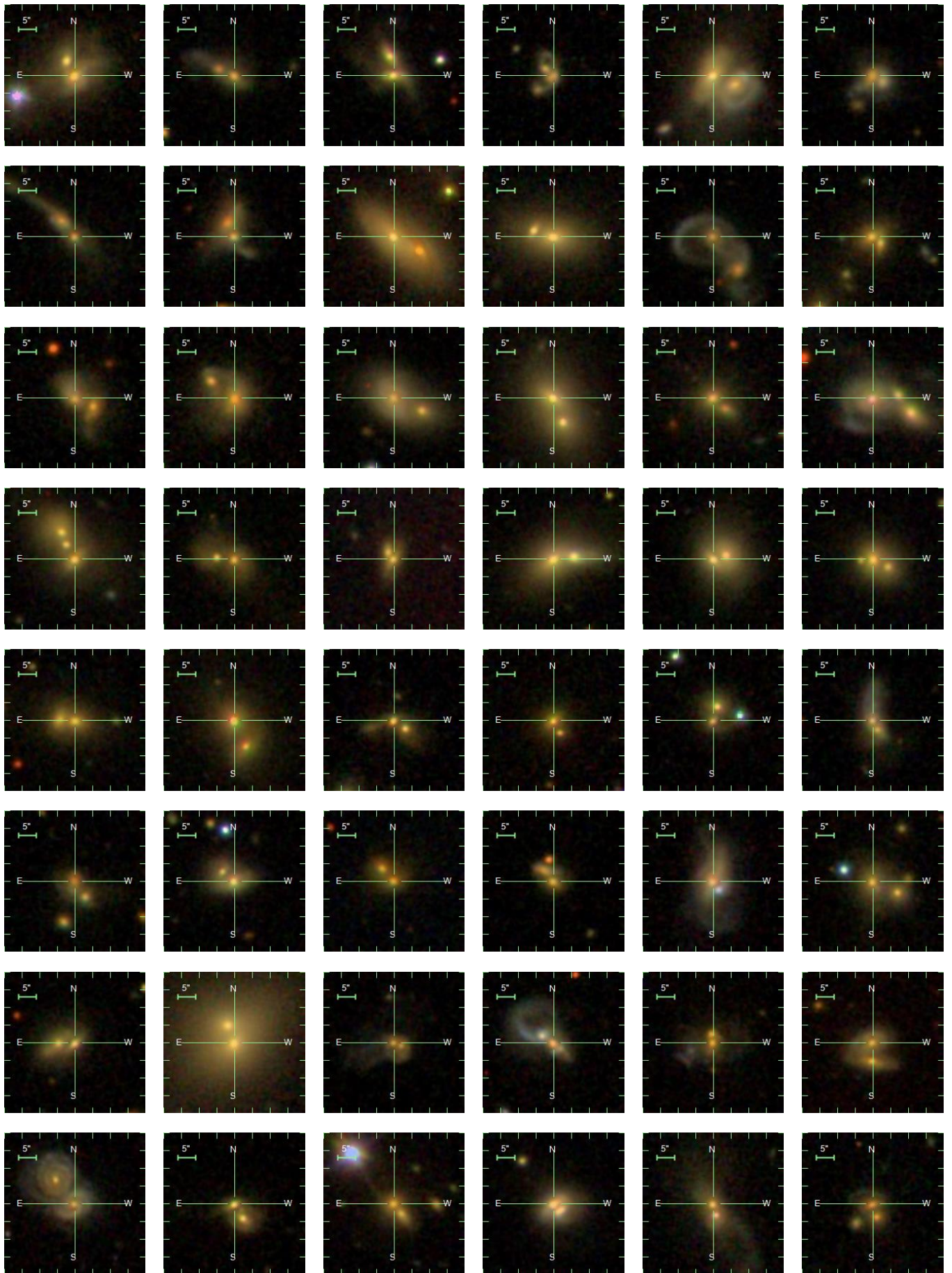


Figure B1. Panel of Discovered DNGs

**Table B2.** Subset of the final reduced sample of double/multiple nuclei in closely interacting galaxies

No.	Comp. No.	Object id	Redshift z	u	g	r	i	z	$M_R$	Class SDSS	Subclass SDSS	Class BPT
1	1	1237645942905700478	0.131	20.84	18.74	17.44	16.78	16.34	-22.6459	GALAXY	...	composite
	2	1237645942905700479	0.131	21.9	19.44	18.09	17.62	17.06	-21.7872	GALAXY	...	...
2	1	1237660636002713767	0.077	19.67	17.57	16.6	16.15	15.81	-21.5264	GALAXY	...	SF
	2	1237660636002713768	0.079	19.61	17.47	16.48	16.01	15.7	-21.8155	GALAXY	AGN	composite
3	1	1237657191979286606	0.087	19.23	17.09	16.06	15.46	15.15	-21.8744	QSO	Starburst	seyfert
	2	1237657191979286607	0.087	19.26	17.28	16.35	15.97	15.59	-21.7874	GALAXY	...	LINER
4	1	1237661465992626516	0.063	19.53	17.53	16.54	16.08	15.72	-21.6477	GALAXY	Broadline	LINER
	2	1237661465992626517	0.065	19.36	17.24	16.22	15.72	15.36	-21.6509	GALAXY	AGN	LINER
5	1	1237661972259537090	0.072	18.89	17.01	16.1	15.61	15.35	-21.7777	QSO	Starburst	seyfert
	2	1237661972259537092	0.072	18.85	17.41	16.68	16.27	15.99	-21.3021	GALAXY	Starforming	SF
6	1	1237662224066740430	0.107	20.19	18.16	17.28	16.83	16.49	-20.5664	GALAXY	AGN	composite
	2	1237662224066740431	0.107	19.04	18.06	17.76	17.48	17.4	-20.0496	GALAXY	Starburst	SF
7	1	1237659133284843796	0.269	19.54	19.06	18.16	17.74	17.36	-22.9486	QSO	Broadline	SF
	2	1237659133284843797	0.27	23.49	20.56	18.74	18.03	17.6	-23.4795	GALAXY	...	LINER
8	1	1237651250968461337	0.223	18.97	18.82	18.39	18.01	17.98	-21.3989	QSO	Starburst	composite
	2	1237651250968461338	0.223	24.15	21.59	20.53	19.98	19.69	-20.8064	GALAXY	Starburst	composite
9	1	1237670965918957796	0.213	21.48	19.66	18.15	17.62	17.27	-22.642	GALAXY	...	seyfert
	2	1237670965918957793	0.208	19.55	19.1	18.38	17.97	17.85	-21.6676	QSO	Starburst	SF
	3	1237670965918957798	0.212	24.18	19.65	18.26	17.65	17.31	-22.1665	GALAXY	...	...
10	1	1237663783680802920	0.025	21.26	20.88	20.82	20.83	20.91	-19.9634	G		
	2	1237663783680802925	0.025	22.57	21.8	22.38	22.24	22.83	-16.276	GSB		
	3	1237663783680802912	0.025	16.65	15.68	15.17	15.04	15.28	-19.9353	GSB		
	4	1237663783680802915	0.025	20.8	20.3	20.59	20.76	21.9	-19.5298	GSB		

Table B3: DAGN sources

No.	Co. No.	obj ID	Z	g	r	Class (SDSS)	Subclass (SDSS)	Class (From BPT)	Comments
1	1	1237650762394959890	0.081	16.61	15.65	GALAXY	BROADLINE	seyfert	...
	2	1237650762394959891	0.081	17.74	16.83	GALAXY	...	composite	...
2	1	1237651250964004981	0.102	18.54	17.51	GALAXY	STARFORMING	composite	...
	2	1237651250964004982	0.102	18.28	17.48	GALAXY	STARBURST	composite	...
3	1	1237651252018151484	0.075	16.48	15.53	GALAXY	...	composite	...
	2	1237651252018151487	0.075	17.12	16.17	GALAXY	...	LINER	...
4	1	1237651252024377492	0.089	17.59	16.62	GALAXY	...	LINER	...
	2	1237651252024377493	0.089	17.77	16.8	GALAXY	...	LINER	...
5	1	1237651273510289469	0.118	16.79	15.75	GALAXY	...	LINER	...
	2	1237651273510289470	0.119	19.02	17.93	GALAXY	...	composite	...
6	1	1237652600110383327	0.166	18.2	17.91	GALAXY	STARFORMING	composite	...
	2	1237652600110383328	0.166	18.53	17.75	GALAXY	...	seyfert	...
7	1	1237652900234133595	0.2	19.19	17.74	GALAXY	...	LINER	...
	2	1237652900234133596	0.198	20.15	19.1	GALAXY	STARFORMING	composite	...
8	1	1237652946379604015	0.166	18.87	17.77	GALAXY	...	composite	...
	2	1237652946379604014	0.164	18.06	16.83	GALAXY	...	LINER	...
9	1	1237653441374453924	0.069	17.21	16.3	GALAXY	STARFORMING	composite	...
	2	1237653441374453925	0.071	16.68	15.71	GALAXY	...	composite	...
10	1	1237654031400566817	0.04	15.89	15.05	GALAXY	...	LINER	...
	2	1237654031400566818	0.04	16.2	15.32	GALAXY	STARFORMING	composite	...
11	1	1237654382516240489	0.125	17.32	16.16	GALAXY	...	LINER	...
	2	1237654382516240490	0.123	17.97	16.98	GALAXY	...	seyfert	...
12	1	1237654880736968887	0.098	17.95	16.98	GALAXY	...	composite	...
	2	1237654880736968888	0.098	18.02	17.33	GALAXY	STARFORMING	composite	...
13	1	1237655106765521018	0.114	17.3	16.26	GALAXY	...	composite	...
	2	1237655106765521019	0.113	18.67	17.82	GALAXY	...	composite	...
14	1	1237655369279733929	0.073	17.8	16.98	GALAXY	STARFORMING	composite	...
	2	1237655369279733928	0.074	16.85	16.07	GALAXY	STARFORMING	composite	...
15	1	1237655465384214778	0.074	16.01	15.07	GALAXY	...	composite	...
	2	1237655465384214780	0.071	18.11	17.19	GALAXY	...	composite	...
16	1	1237655465920364786	0.098	18.02	17.06	GALAXY	...	seyfert	...
	2	1237655465920364787	0.098	18.98	18.04	GALAXY	...	composite	...
17	1	1237655495979106559	0.091	18.24	17.34	GALAXY	...	LINER	...
	2	1237655495979106560	0.09	18.01	17.03	GALAXY	STARFORMING	composite	...
18	1	1237655692474515647	0.175	17.94	16.58	GALAXY	...	LINER	...
	2	1237655692474515648	0.174	18.99	17.86	GALAXY	...	composite	...
19	1	1237656239009104192	0.134	18.57	17.51	GALAXY	...	LINER	...
	2	1237656239009104193	0.133	18.5	17.29	GALAXY	...	LINER	...
20	1	1237656567582294307	0.027	16.53	15.54	GALAXY	...	composite	...
	2	1237656567582294308	0.026	17.06	16.24	GALAXY	...	composite	...
21	1	1237667253455356213	0.09	16.54	15.45	GALAXY	...	composite	...
	2	1237667253455356214	0.091	20.2	19.36	GALAXY	...	LINER	...
22	1	1237656567585833094	0.057	15.92	14.97	GALAXY	...	LINER	...
	2	1237656567585833097	0.057	17.11	15.8	GALAXY	...	seyfert	...
23	1	1237656906354393114	0.023	14.84	14.01	GALAXY	...	LINER	...
	2	1237656906354393115	0.024	20.86	20.73	GALAXY	STARFORMING	composite	...
24	1	1237657189817516083	0.139	18.87	17.63	GALAXY	...	LINER	...
	2	1237657189817516085	0.138	19.38	18.3	GALAXY	...	composite	...
25	1	1237657221485625353	0.046	15.08	14.24	GALAXY	BROADLINE	LINER	...
	2	1237657221485559856	0.046	17.52	16.67	GALAXY	...	LINER	...
26	1	1237657609104982532	0.153	18.17	17.06	GALAXY	...	seyfert	...
	2	1237657609104982533	0.153	19.09	17.89	GALAXY	...	LINER	...
27	1	1237657612874940605	0.07	17.27	16.32	GALAXY	...	composite	...
	2	1237657612874940607	0.069	18.41	17.55	GALAXY	...	composite	...
28	1	1237657628432531602	0.078	16.75	15.74	GALAXY	BROADLINE	LINER	...
	2	1237657628432531603	0.078	18.11	17.13	GALAXY	...	composite	...

29	1	1237657857148911724	0.06	17.54	16.73	GALAXY	...	LINER	...
	2	1237657857148911725	0.06	16.83	16	GALAXY	...	composite	...
30	1	1237658300056338796	0.139	17.24	16.34	GALAXY	STARFORMING	LINER	...
	2	1237658300056338797	0.138	17.93	16.99	GALAXY	...	composite	...
31	1	1237658424090493080	0.072	17.56	16.62	GALAXY	STARFORMING	composite	...
	2	1237658424090493081	0.071	17.17	16.23	GALAXY	...	composite	...
32	1	1237658611440222364	0.144	18.18	16.99	GALAXY	...	LINER	...
	2	1237658611440222365	0.145	18.7	17.62	GALAXY	...	composite	...
33	1	1237658918533005504	0.113	18.26	17.27	GALAXY	...	seyfert	...
	2	1237658918533005505	0.113	18.78	17.87	GALAXY	...	composite	...
34	1	1237659119862939753	0.144	17.32	16.44	GALAXY	STARFORMING	composite	...
	2	1237659119862939754	0.145	18.47	17.18	GALAXY	...	seyfert	...
35	1	1237659119864774675	0.099	16.98	15.84	GALAXY	...	composite	...
	2	1237659119864774676	0.1	18.46	17.43	GALAXY	...	seyfert	...
36	1	1237659132206448648	0.11	18.89	17.87	GALAXY	...	seyfert	...
	2	1237659132206448651	0.11	19.81	18.81	GALAXY	...	seyfert	...
37	1	1237660240313385134	0.142	19.36	18.23	GALAXY	...	LINER	...
	2	1237660240313385135	0.142	18.66	17.75	GALAXY	STARFORMING	composite	...
38	1	1237660240313712760	0.038	15.09	14.22	GALAXY	STARFORMING	LINER	...
	2	1237660240313712761	0.038	19.4	18.63	GALAXY	...	composite	...
39	1	1237660241385029806	0.074	17.26	16.32	GALAXY	BROADLINE	LINER	...
	2	1237660241385029810	0.073	18.49	17.54	GALAXY	...	composite	...
40	1	1237660669282812044	0.115	18.74	17.73	GALAXY	...	LINER	...
	2	1237660669282812045	0.116	18.87	17.85	GALAXY	...	seyfert	...
41	1	1237660963472932915	0.048	16.06	15.01	GALAXY	...	LINER	...
	2	1237660963472932916	0.048	16.39	15.57	GALAXY	STARFORMING	composite	...
42	1	1237661086415585604	0.047	14	13.14	GALAXY	...	LINER	...
	2	1237661086415585607	0.048	17.66	15.61	GALAXY	...	composite	...
43	1	1237661137963254106	0.129	17.68	16.6	GALAXY	...	LINER	...
	2	1237661137963254107	0.129	18.95	17.83	GALAXY	...	LINER	...
44	1	1237661151377424586	0.104	17.78	16.58	GALAXY	...	composite	...
	2	1237661151377424587	0.104	18.62	17.73	GALAXY	...	seyfert	...
45	1	1237661352706179107	0.082	16.61	15.82	GALAXY	...	composite	...
	2	1237661352706179108	0.082	17.79	16.8	GALAXY	...	composite	...
46	1	1237661382778093715	0.069	16.2	15.3	GALAXY	...	composite	...
	2	1237661382778093716	0.068	16.93	16.04	GALAXY	BROADLINE	composite	...
47	1	1237661418748444829	0.107	17.06	16.09	GALAXY	...	LINER	...
	2	1237661418748444830	0.107	17.91	16.95	GALAXY	...	seyfert	...
48	1	1237661812274233471	0.064	16.26	15.59	GALAXY	STARBURST	composite	...
	2	1237661812274233472	0.064	17.36	16.41	GALAXY	...	LINER	...
49	1	1237661813348106331	0.123	17.69	16.67	GALAXY	...	seyfert	...
	2	1237661813348106332	0.124	18.72	17.74	GALAXY	...	composite	...
50	1	1237661850411204729	0.076	16.56	15.75	GALAXY	STARFORMING	composite	...
	2	1237661850411204730	0.075	17.42	16.5	GALAXY	...	seyfert	...
51	1	1237661871330361452	0.112	17.41	16.36	GALAXY	...	LINER	...
	2	1237661871330361453	0.112	16.78	15.77	GALAXY	...	composite	...
52	1	1237661957762842806	0.133	18.39	17.21	GALAXY	...	composite	...
	2	1237661957762842807	0.133	18.38	17.34	GALAXY	...	seyfert	...
53	1	1237661966886633584	0.131	18.37	17.27	GALAXY	...	LINER	...
	2	1237661966886633585	0.131	18.68	17.6	GALAXY	...	LINER	...
54	1	1237661971721945220	0.073	17.2	16.23	GALAXY	...	seyfert	...
	2	1237661971721945221	0.074	16.58	15.72	GALAXY	...	LINER	...
55	1	1237662193453760669	0.171	18.79	17.6	GALAXY	...	composite	...
	2	1237662193453760670	0.173	18.82	17.62	GALAXY	...	seyfert	...
56	1	1237662194541002843	0.073	16.41	15.47	GALAXY	...	LINER	...
	2	1237662194541002844	0.074	16.61	15.8	GALAXY	...	seyfert	...
57	1	1237662198280552769	0.172	18.85	17.62	GALAXY	...	LINER	...
	2	1237662198280552768	0.172	18.94	17.69	GALAXY	...	LINER	...

58	1	1237662225666932750	0.099	17.88	16.83	GALAXY	...	composite	...
	2	1237662225666932751	0.099	19.04	18.21	GALAXY	...	composite	...
59	1	1237662335178178801	0.065	16.5	15.57	GALAXY	...	seyfert	...
	2	1237662335178178802	0.065	17.95	17.05	GALAXY	...	seyfert	...
60	1	1237662336792920258	0.069	17.12	16.25	GALAXY	...	LINER	...
	2	1237662336792920257	0.07	16.53	15.67	GALAXY	STARFORMING	composite	...
61	1	1237662474231021741	0.117	17.17	16.09	GALAXY	...	LINER	...
	2	1237662474231021742	0.117	18.18	17.23	GALAXY	...	composite	...
62	1	1237662498390737019	0.154	17.83	16.69	GALAXY	...	LINER	...
	2	1237662498390737020	0.153	18.12	16.95	GALAXY	...	LINER	...
63	1	1237662200436752504	0.105	17.14	16.09	GALAXY	...	LINER	...
	2	1237662636375867758	0.105	17.9	16.8	GALAXY	STARFORMING	composite	...
64	1	1237662640123609565	0.059	16.41	15.48	GALAXY	...	composite	...
	2	1237662640123609566	0.06	22.5	21.75	GALAXY	...	composite	...
65	1	1237663463145537628	0.084	14.96	13.92	GALAXY	...	seyfert	...
	2	1237663463145537634	0.084	17.17	16.97	GALAXY	...	LINER	...
66	1	1237663543683318057	0.084	17.98	17.1	GALAXY	...	composite	...
	2	1237663543683318058	0.085	18.68	17.93	GALAXY	STARFORMING	composite	...
67	1	1237663782589432032	0.139	18.93	17.8	GALAXY	...	composite	...
	2	1237663782589432033	0.139	18.87	17.8	GALAXY	...	composite	...
68	1	1237663783122370706	0.186	18.56	17.25	GALAXY	...	LINER	...
	2	1237663783122370707	0.183	19.95	18.77	GALAXY	...	LINER	...
69	1	1237663783131283514	0.089	16.95	16.52	GALAXY	STARBURST	composite	...
	2	1237663783131283515	0.089	17.46	16.59	GALAXY	...	composite	...
70	1	1237663783136985126	0.12	18.76	17.85	GALAXY	...	composite	...
	2	1237663783136985125	0.121	18.08	17.05	GALAXY	...	seyfert	...
71	1	1237663783674183846	0.112	18.22	17.25	GALAXY	STARFORMING	composite	...
	2	1237663783674183847	0.111	18.5	18.01	GALAXY	STARFORMING	composite	...
72	1	1237663784195653787	0.079	18.56	17.53	GALAXY	...	LINER	...
	2	1237663784195653788	0.079	18.15	17.67	GALAXY	...	composite	...
73	1	1237663784200831188	0.073	17.56	16.65	GALAXY	...	LINER	...
	2	1237663784200831189	0.074	18.31	17.48	GALAXY	STARFORMING	composite	...
74	1	1237663784739995886	0.115	17.53	16.79	GALAXY	STARFORMING	composite	...
	2	1237663784739995887	0.116	18.39	17.38	GALAXY	...	composite	...
75	1	1237664291548823599	0.041	16.03	15.17	GALAXY	BROADLINE	LINER	...
	2	1237664291548823600	0.041	14.75	13.92	GALAXY	...	LINER	...
76	1	1237664667352039631	0.084	18.05	17.08	GALAXY	...	LINER	...
	2	1237664667352039632	0.085	17.56	16.84	GALAXY	STARFORMING	LINER	...
77	1	1237664817676484746	0.215	18.67	17.79	GALAXY	STARFORMING	composite	...
	2	1237664817676484748	0.216	18.88	17.84	GALAXY	STARFORMING	composite	...
78	1	1237664871900577858	0.049	17.32	16.45	GALAXY	...	LINER	...
	2	1237664871900577859	0.051	17.96	17.07	GALAXY	...	seyfert	...
79	1	1237664877803077714	0.116	18.6	17.59	GALAXY	...	LINER	...
	2	1237664877803077715	0.118	18.47	17.43	GALAXY	...	LINER	...
80	1	1237664877807927453	0.206	19	17.68	GALAXY	...	seyfert	...
	2	1237664877807927454	0.207	18.92	17.62	GALAXY	...	LINER	...
81	1	1237665103283814519	0.075	17.47	16.54	GALAXY	...	LINER	...
	2	1237665103283814520	0.075	16.45	15.57	GALAXY	...	LINER	...
82	1	1237665129610936526	0.154	18.7	17.56	GALAXY	...	LINER	...
	2	1237665129610936527	0.153	18.88	17.89	GALAXY	STARFORMING	composite	...
83	1	1237665328779100316	0.154	18.79	17.63	GALAXY	...	LINER	...
	2	1237665328779100317	0.155	18.15	16.98	GALAXY	...	seyfert	...
84	1	1237665330927435873	0.088	17.43	16.48	GALAXY	STARBURST	composite	...
	2	1237665330927435875	0.088	18.99	18.25	GALAXY	...	seyfert	...
85	1	1237665331455459378	0.072	16.66	15.84	GALAXY	STARFORMING	seyfert	...
	2	1237665331455459379	0.073	17.42	17.16	GALAXY	STARFORMING	composite	...
86	1	1237665331457425465	0.128	17.77	16.62	GALAXY	...	LINER	...
	2	1237665331457425466	0.127	18	16.8	GALAXY	...	LINER	...

87	1	1237665428091240506	0.14	17.25	16.27	GALAXY	...	seyfert	...
	2	1237665428091240507	0.141	19.37	18.32	GALAXY	...	composite	...
88	1	1237665429713780966	0.088	18.43	17.5	GALAXY	...	composite	...
	2	1237665429713846350	0.09	17.52	16.57	GALAXY	...	LINER	...
89	1	1237665440439336990	0.065	15.47	14.57	GALAXY	...	composite	...
	2	1237665440439336991	0.061	15.71	14.82	GALAXY	...	LINER	...
90	1	1237665531723579489	0.132	17.42	16.37	GALAXY	...	LINER	...
	2	1237665531723579490	0.13	18.17	17.16	GALAXY	...	LINER	...
91	1	1237665566082269200	0.094	16.75	15.76	GALAXY	...	LINER	...
	2	1237665566082269201	0.094	18.19	17.2	GALAXY	...	composite	...
92	1	1237666185634447638	0.121	18.79	17.64	GALAXY	...	LINER	...
	2	1237666185634447639	0.121	18.52	17.3	GALAXY	...	LINER	...
93	1	1237666301627924604	0.156	20.86	19.58	GALAXY	...	composite	...
	2	1237666301627924605	0.156	17.89	16.97	GALAXY	STARFORMING	LINER	...
94	1	1237666407381598382	0.08	18.01	17.08	GALAXY	STARFORMING	composite	...
	2	1237666407381598383	0.08	16.91	16.49	GALAXY	...	composite	...
95	1	1237667109574279383	0.201	18.89	17.51	GALAXY	...	LINER	...
	2	1237667109574279384	0.2	19.12	17.79	GALAXY	...	composite	...
96	1	1237667209974710300	0.078	17.88	17.4	GALAXY	STARBURST	composite	...
	2	1237667209974710301	0.078	17.72	16.83	GALAXY	STARFORMING	composite	...
97	1	1237667212115050866	0.172	18.79	17.51	GALAXY	...	LINER	...
	2	1237667212115050867	0.173	19.53	18.38	GALAXY	...	composite	...
98	1	1237667212136284360	0.138	18.89	17.71	GALAXY	...	LINER	...
	2	1237667212136284359	0.13	17.88	17.03	GALAXY	...	seyfert	...
99	1	1237667253453324693	0.141	17.65	16.64	GALAXY	...	LINER	...
	2	1237667253453324694	0.141	18.28	17.11	GALAXY	...	LINER	...
100	1	1237667254546006103	0.145	18.31	17.88	GALAXY	STARFORMING	composite	...
	2	1237667254546006104	0.145	18.64	17.84	GALAXY	...	LINER	...
101	1	1237667323250213040	0.038	16.18	15.28	GALAXY	STARFORMING	composite	...
	2	1237667323250213041	0.038	18.34	18	GALAXY	...	composite	...
102	1	1237667323796127885	0.083	17.01	16.18	GALAXY	...	LINER	...
	2	1237667323796127886	0.083	18.27	17.47	GALAXY	STARFORMING	composite	...
103	1	1237667442437914759	0.079	17.58	16.64	GALAXY	...	LINER	...
	2	1237667442437914760	0.08	17.55	16.73	GALAXY	STARFORMING	composite	...
104	1	1237667549268148435	0.118	17.52	16.73	GALAXY	STARFORMING	composite	...
	2	1237667549268213959	0.116	17.25	16.43	GALAXY	STARFORMING	composite	...
105	1	1237667733989949671	0.09	18.33	17.36	GALAXY	...	composite	...
	2	1237667733989949676	0.089	18.26	17.31	GALAXY	...	seyfert	...
106	1	1237667734526886197	0.119	18.69	17.65	GALAXY	...	composite	...
	2	1237667734526886198	0.118	18.11	17.08	GALAXY	...	seyfert	...
107	1	1237667736133828618	0.096	16.91	15.97	GALAXY	...	seyfert	...
	2	1237667736133828619	0.097	17.06	16.07	GALAXY	...	LINER	...
108	1	1237667781774934219	0.102	16.8	15.87	GALAXY	...	composite	...
	2	1237667781774934220	0.103	18.28	17.3	GALAXY	...	seyfert	...
109	1	1237667783883817113	0.148	18.42	17.24	GALAXY	...	LINER	...
	2	1237667783883817114	0.149	18.71	17.55	GALAXY	...	seyfert	...
110	1	1237667783929299179	0.051	15.52	14.64	GALAXY	BROADLINE	LINER	...
	2	1237667783929299180	0.05	16.51	15.66	GALAXY	BROADLINE	LINER	...
111	1	1237667910069190795	0.077	16.79	16.11	GALAXY	STARFORMING	composite	...
	2	1237667910069190796	0.077	16.94	16.16	GALAXY	STARFORMING	composite	...
112	1	1237667916494012508	0.066	16.64	15.76	GALAXY	...	seyfert	...
	2	1237667916494012509	0.065	16.66	15.76	GALAXY	...	LINER	...
113	1	1237668271362211975	0.088	17.3	16.28	GALAXY	...	LINER	...
	2	1237668271362211976	0.089	17.94	17.1	GALAXY	...	LINER	...
114	1	1237668298204446938	0.119	17.77	17.09	GALAXY	STARBURST	composite	...
	2	1237668298204446939	0.119	17.98	16.93	GALAXY	STARFORMING	composite	...
115	1	1237668589722534078	0.153	18.66	17.59	GALAXY	STARFORMING	composite	...
	2	1237668589722534074	0.152	19.15	17.98	GALAXY	...	composite	...

116	1	1237668623551103255	0.216	18.75	17.72	GALAXY	...	composite	...
	2	1237668623551103256	0.216	20.54	18.94	GALAXY	...	composite	...
117	1	1237668672938115205	0.136	17.47	16.4	GALAXY	...	LINER	...
	2	1237668672938115206	0.135	18.91	17.89	GALAXY	...	composite	...
118	1	1237670964313456852	0.076	16.11	15.16	GALAXY	...	LINER	...
	2	1237670964313456853	0.078	16.55	15.61	GALAXY	...	LINER	...
119	1	1237670965383266430	0.031	15.93	15.04	GALAXY	...	LINER	...
	2	1237670965383266433	0.03	16.39	15.57	GALAXY	...	composite	...
120	1	1237671931208925416	0.073	16.19	15.26	GALAXY	...	LINER	...
	2	1237671931208925417	0.073	17.76	16.78	GALAXY	...	LINER	...
121	1	1237673807580693064	0.144	17.59	16.39	GALAXY	...	LINER	...
	2	1237673807580693069	0.14	18.43	17.37	GALAXY	...	composite	...
122	1	1237673808116122327	0.1	16.93	16.19	GALAXY	STARFORMING	composite	...
	2	1237673808116122329	0.099	17.35	16.4	GALAXY	...	LINER	...
123	1	1237674649921061067	0.096	17.12	16.11	GALAXY	...	composite	...
	2	1237674649921061068	0.093	17.3	16.32	GALAXY	...	composite	...
124	1	1237657587096289353	0.025	14.72	13.89	GALAXY	...	seyfert	...
	2	1237657587096289354	0.025	18.77	18.21	GALAXY	...	seyfert	...
125	1	1237666210341978625	0.06	17.66	16.97	GALAXY	STARFORMING	composite	...
	2	1237666210341978627	0.061	17.13	16.36	GALAXY	STARFORMING	composite	...
126	1	1237662335180341316	0.064	16.61	15.84	GALAXY	STARFORMING	composite	...
	2	1237662335180341327	0.064	21.32	21.88	GALAXY	STARFORMING	composite	...
127	1	1237659327092752463	0.149	18.12	17.52	QSO	STARBURST	seyfert	...
	2	1237659327092752464	0.15	18.58	17.62	GALAXY	STARFORMING	composite	...
128	1	1237667915957665832	0.065	15.74	14.74	GALAXY	...	composite	...
	2	1237667915957665835	0.065	16.17	15.24	GALAXY	AGN	composite	...
129	1	1237668588651282620	0.074	16.46	15.57	GALAXY	...	LINER	...
	2	1237668588651282621	0.074	16.61	15.76	GALAXY	AGN	LINER	...
130	1	1237671262267506768	0.052	14.94	14.02	GALAXY	AGN	LINER	...
	2	1237671262267506767	0.053	17.55	16.73	GALAXY	...	LINER	...
131	1	1237666227490586650	0.103	17.04	16.29	GALAXY	STARBURST	composite	...
	2	1237666227490586649	0.104	18.98	17.95	QSO	STARBURST	composite	...
132	1	1237666228063371544	0.1	18.03	16.97	GALAXY	AGN	seyfert	...
	2	1237666228063371545	0.099	16.91	16.08	GALAXY	STARFORMING	composite	...
133	1	1237667252917895553	0.153	17.7	16.48	GALAXY	...	LINER	...
	2	1237667252917895554	0.156	17.78	16.94	QSO	STARBURST	composite	...
134	1	1237664667360755820	0.152	19.07	18.03	QSO	STARBURST	composite	...
	2	1237664667360755822	0.153	19.56	19.29	GALAXY	AGN	composite	...
135	1	1237660240314433647	0.156	18.85	17.5	GALAXY	...	seyfert	...
	2	1237660240314433648	0.158	19.23	18.07	GALAXY	AGN	seyfert	...
136	1	1237655502962688659	0.03	15.96	15.16	GALAXY	AGN	LINER	...
	2	1237655502962688660	0.029	19.28	18.1	GALAXY	STARFORMING	composite	...
137	1	1237655465916104829	0.132	18.21	17.28	GALAXY	AGN	LINER	...
	2	1237655465916104830	0.132	18.69	17.5	GALAXY	...	LINER	...
138	1	1237653616938516591	0.099	17.12	16.19	GALAXY	AGN	LINER	...
	2	1237653616938516592	0.099	17.8	16.84	GALAXY	...	LINER	...
139	1	1237652600635851575	0.175	18.06	17.01	GALAXY	AGN	LINER	...
	2	1237652600635851576	0.178	18.44	17.13	GALAXY	...	LINER	...
140	1	1237651250968461337	0.223	18.82	18.39	QSO	STARBURST	composite	...
	2	1237651250968461338	0.223	21.59	20.53	GALAXY	STARBURST	composite	...
141	1	1237648721245503520	0.047	17.75	17.16	GALAXY	STARBURST	composite	...
	2	1237648721245503521	0.048	16.32	15.52	GALAXY	AGN	seyfert	...
142	1	1237648722312888376	0.138	17.81	17.16	GALAXY	STARBURST	seyfert	...
	2	1237648722312888377	0.138	17.9	17.08	GALAXY	AGN	seyfert	...
143	1	1237654382514471111	0.06	16.93	16.18	GALAXY	AGN	seyfert	...
	2	1237654382514471112	0.06	17.83	17.05	GALAXY	STARFORMING	composite	...
144	1	1237657191979286606	0.087	17.09	16.06	QSO	STARBURST	seyfert	...
	2	1237657191979286607	0.087	17.28	16.35	GALAXY	...	LINER	...

145	1	1237659326018355482	0.105	17.67	16.7	GALAXY	...	seyfert	...
	2	1237659326018355483	0.107	18.54	17.54	GALAXY	AGN	seyfert	...
146	1	1237661465992626516	0.063	17.53	16.54	GALAXY	BROADLINE	LINER	...
	2	1237661465992626517	0.065	17.24	16.22	GALAXY	AGN	LINER	...
147	1	1237661812275347597	0.091	17.72	16.87	GALAXY	AGN	seyfert	...
	2	1237661812275347598	0.092	18.67	17.72	GALAXY	...	composite	...
148	1	1237661813885436021	0.065	17.04	16.11	GALAXY	...	LINER	...
	2	1237661813885436022	0.065	17.62	16.79	GALAXY	AGN	seyfert	...
149	1	1237662224058089529	0.087	17.6	16.6	GALAXY	...	composite	...
	2	1237662224058024149	0.088	17.72	16.77	GALAXY	AGN	LINER	...
150	1	1237663542609117199	0.128	18.59	17.38	QSO	STARBURST	seyfert	...
	2	1237663542609117200	0.128	18.23	17.11	GALAXY	...	composite	...
	1	1237661064950710579	0.126	17.12	16.03	GALAXY	...	composite	Third source have
151	2	1237661064950710580	0.125	17.75	16.71	GALAXY	...	LINER	insufficient Line
	3	1237661064950710581	0.127	19.92	18.91	GALAXY	...	...	emission data
152	1	1237663275777392799	0.094	19.14	18.1	GALAXY	...	composite	Dual AGN with an
	2	1237663275777392800	0.095	17.14	16.13	GALAXY	...	seyfert	associated SF nuclei
	3	1237663275777392798	0.091	18.57	17.53	GALAXY	...	SF	
153	1	1237663542608920721	0.144	18.8	17.59	GALAXY	...	LINER	Dual AGN with an
	2	1237663542608920724	0.144	21.45	20.2	GALAXY	...	seyfert	associated SF nuclei
	3	1237663542608920720	0.144	19.02	17.82	GALAXY	...	SF	
154	1	1237663783126237343	0.063	17.49	16.54	GALAXY	...	composite	Dual AGN with
	2	1237663783126237344	0.064	17.41	16.44	GALAXY	...	LINER	associated SF nuclei
	3	1237663783126237342	0.064	16.26	15.34	GALAXY	...	SF	
155	1	1237665564997714246	0.26	19.69	18.18	GALAXY	...	LINER	Third source have
	2	1237665564997779740	0.254	18.33	16.69	GALAXY	...	composite	insufficient Line
	3	1237665564997714249	0.254	19.71	18.2	GALAXY	...	...	emission data
156	1	1237668299280089194	0.063	16.34	15.41	GALAXY	...	LINER	Third source have
	2	1237668299280089196	0.063	17.68	16.93	GALAXY	STARFORMING	composite	insufficient Line
	3	1237668299280089195	0.062	16.64	15.73	GALAXY	...	...	emission data
157	1	1237666301093675376	0.086	17.55	16.76	QSO	BROADLINE	LINER	Dual AGN with 2
	2	1237666301093675377	0.087	19.04	18.27	GALAXY	...	LINER	associated SF nuclei
	3	1237666301093675378	0.088	18.5	17.87	GALAXY	STARBURST	SF	
	4	1237666301093675379	0.086	19.47	18.99	GALAXY	STARFORMING	SF	
158	1	1237657192517926989	0.105	18.33	17.34	GALAXY	...	LINER	Triple AGN
	2	1237657192517926990	0.106	19.83	18.94	GALAXY	...	LINER	
	3	1237657192517926993	0.106	17.87	16.88	GALAXY	...	seyfert	
159	1	1237667736133107729	0.102	17.07	16.05	GALAXY	...	seyfert	Triple AGN (Third source
	2	1237667736133107730	0.103	17.02	15.96	GALAXY	...	LINER	had insufficient emission line data
	3	1237667736133107731	0.103	17.8	16.84	GALAXY	BROADLINE	...	but is classified under subclass Broadline in SDSS)